Chapter 4

The BTeV Baseline Detector

In this chapter, we describe the BTeV detector baseline design. We begin with a review of the important characteristics of hadronic B production and the properties of the Tevatron which influence the design. We then give a description of the C0 Collision Hall and IR. We discuss each major component of the detector in turn, including the key requirements that drive the design, the choice of the baseline technology, the expected performance, and the options which are still under consideration. More details on each major component are presented in later chapters.

4.1 Characteristics of Hadronic b Production

The kinematics of hadronic B and charm production play a major role in the design of BTeV. We review the most important features here.

It is customary to characterize heavy quark production in hadron collisions with the two variables p_t and η. The latter variable was first invented by those who studied high energy cosmic rays and is assigned the value

$$\eta = -ln\left(\tan\left(\theta/2\right)\right), \tag{4.1}$$

where θ is the angle of the particle with respect to the beam direction.

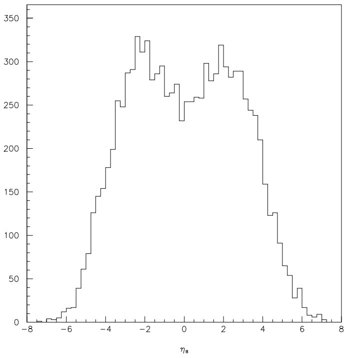

Figure 4.1: The B yield versus η.

According to QCD calculations of b quark production, the b's are produced "uniformly" in η and have a truncated transverse momentum, p_t, spectrum, characterized by a mean value approximately equal to the B mass [1]. The distribution in η is shown in Fig. 4.1.

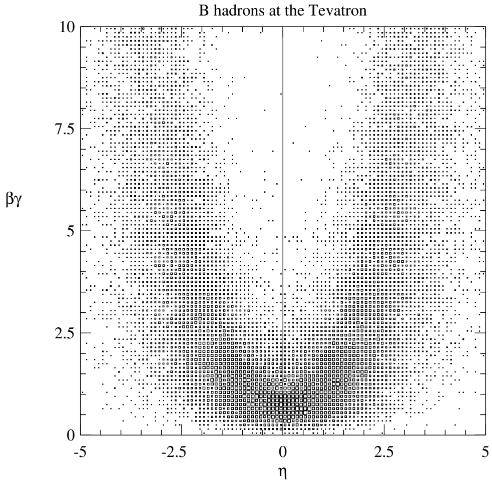

Figure 4.2: $\beta\gamma$ of the B versus η.

There is a strong correlation between the B momentum and η. Shown in Fig. 4.2 is the $\beta\gamma$ of the B hadron versus η from Pythia at $\sqrt{s}\ =\ 2$ TeV. It can clearly be seen that near η of zero, $\beta\gamma \approx 1$, while at larger values of $|\eta|$, $\beta\gamma$ can easily reach values of 6. This is important because the observed decay length varies with $\beta\gamma$ and furthermore the absolute momenta of the decay products are larger allowing for a suppression of the multiple scattering error.

Since the detector design is somewhat dependent on the Monte Carlo generated b production distributions, it is important to check that the correlations between the b and the $\overline{b}$ are adequately reproduced. Fig. 4.3 shows the azimuthal opening angle distribution between a muon from a b quark decay and the $\bar{b}$ jet as measured by CDF [2] and compares it with the MNR predictions [3].

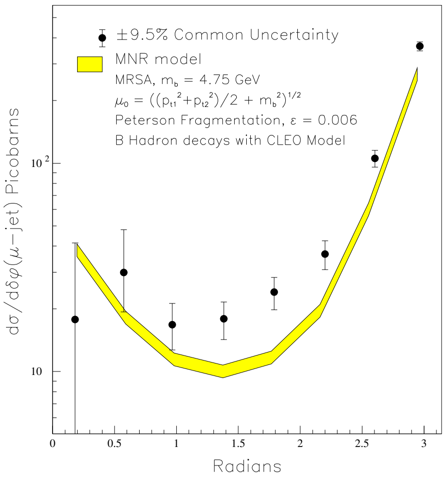

Figure 4.3: The differential $\delta\phi$ cross-sections for p_T^{μ} > 9 GeV/c, $|\eta^{\mu}|$ <0.6, $E_T^{\bar{b}}$ >10 GeV, $\left|\eta^{\bar{b}}\right| < 1.5$ compared with theoretical predictions. The data points have a common systematic uncertainty of $\pm 9.5\%$. The uncertainty in the theory curve arises from the error on the muonic branching ratio and the uncertainty in the fragmentation model.

The model does a good job representing the shape, which shows a strong back-to-back correlation. The normalization is about a factor of two higher in the data than the theory, which is generally true of CDF b cross-section measurements [4]. In hadron colliders all B species, B^o, B^+, B_s^o, b-baryons, and even B_c mesons, are produced at the same time.

The "flat" η distribution hides an important correlation of $b\bar{b}$ production at hadronic colliders. In Fig. 4.4 the production angle of the hadron containing the b quark is plotted versus the production angle of the hadron containing the $\bar{b}$ quark. Here zero degrees represents the direction of the incident proton and 180 degrees, the incident anti-proton. There is a very strong correlation in the proton or the anti-proton directions: when the B is forward the $\overline{B}$ is also forward. (We call both the proton and anti-proton directions forward.) This correlation between B and $\overline{B}$ production is not present in the central region (near 90 degrees). By instrumenting a relatively small region of angular phase space, a large number of $b\bar{b}$ pairs can be detected. Furthermore, the B's populating the forward regions have large values of $\beta\gamma$ and this permits more accurate separation of the primary and secondary vertices and better overall detection efficiency for b hadrons. In addition, the techniques for particle identification in this kinematic range are very well developed. Powerful particle identification is a key to high sensitivity bottom and charm experiments. For these reasons, we have designed a detector with ‘forward coverage’.

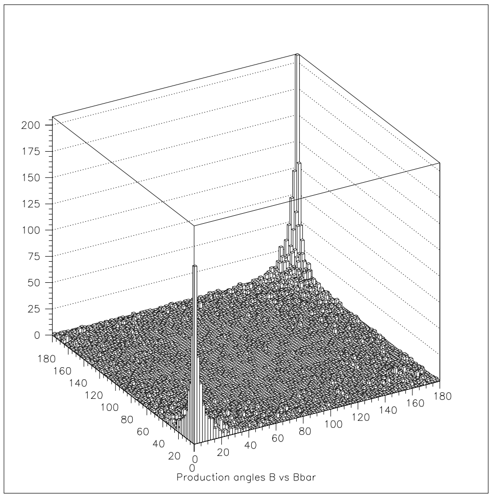

Figure 4.4: The production angle (in degrees) for the hadron containing a b quark plotted versus the production angle for a hadron containing $\bar{b}$ quark, from the Phythia Monte Carlo generator.

Charm production is similar to b production but has a much larger cross section. Current theoretical estimates are that charm is 1-2% of the total $p\bar{p}$ cross-section. The cross section is even more strongly peaked in the forward directions because the average transverse momentum is of the order of only 1.5 GeV/c. The charm cross section has never been measured because texperiments with good acceptance in the central region have very low efficiency for triggering and reconstructing charm. The favorable kinematics in the forward direction gives BTeV a very high efficiency for reconstructing charm.

Table 4.1 gives the relevant Tevatron parameters. We expect to start serious data taking in Fermilab Run II with a luminosity of about $5 \times 10^{31}\mathrm{cm}^{-2}\mathrm{s}^{-1}$; our ultimate luminosity goal, to be obtained in Run III, is $2 \times 10^{32}\mathrm{cm}^{-2}\mathrm{s}^{-1}$.

While BTeV is designed to study $p\bar{p}$ collisions at 2 TeV, it can also run in ‘Fixed Target’ mode. In that mode, a thin wire is inserted into the halo of the circulating beam and the detector studies the collisions of 800 GeV/c protons (or anti-protons) with the nuclei of the wire. For this reason, Fixed Target mode is also referred to as ‘wire mode’.

In this mode, particles diffusing laterally out of the beam eventually reach the wire target where they can interact. Since the diffusion is very slow, each particle will traverse the wire many times until it either interacts or multiple scattering blows its orbit up so badly that it escapes from the machine aperture altogether. We are learning from accelerator physicists what overall interaction rate we can expect.

The cross section for fixed target charm production on a proton at 800 GeV/c is about 30 μb. While this is much lower than in the collider, there are some advantages: first, it

Table 4.1: The Tevatron as a b and c source for BTeV

Luminosity (BTeV design)	$2 \times 10^{32}\text{cm}^{-2}\text{s}^{-1}$
b cross-section	100μb
# of b's per 10^7 sec (Run II)	4×10^{11}
$\frac{\sigma_{b-\bar{b}}}{\sigma_{inel}}$	0.2%
c cross-section	$> 500\ \mu$b
Bunch spacing	132 ns
Luminous region length	$\sigma_z = 30$ cm
Luminous region length	$\sigma_x\ \sigma_y = \approx 50\ \mu$m
Interactions/crossing	$< 2.0 >$

may not require low-β quadrupoles to be installed so it might be available to us earlier than collider mode; second, it is not expected to affect the luminosity at B0 or D0, which is not the case when the beams collide at C0 and this will translate into longer running times; the region along the beam that has to be instrumented with precision vertex detectors is much smaller which means that a small scale vertex detector prototype is all that is needed for initial experiments; and the fact that the center of mass is boosted towards the spectrometer increases the acceptance. However, this mode is not useful to us for B-physics studies because the cross section is of order 10 nb. While we believe that the most sensitive charm experiment will be using the collider, this mode does give us the opportunity to do physics early with a partially instrumented detector.

Bibliography

[1] M. Artuso, "Experimental Facilities for b-Quark Physics," in *B Decays* revised 2nd Edition, Ed. S. Stone, World Scientific, Singapore (1994).

[2] F. Abe *et al*, *Phys. Rev.* D **53**, 1051 (1996).

[3] M. Mangano, P. Nason and G. Ridolfi, *Nucl. Phys.* B **373**, 295 (1992).

[4] F. Abe *et al*, *Phys. Rev. Lett.* **75**, 1451 (1995). Previous UA1 measurements agreed with the theoretical predictions, see C. Albajar *et al*, *Phys. Lett.* B **256**, 121 (1991). Recent D0 measurements agree with both the CDF measurements and the high side of the theoretically allowed range. See S. Abachi *et al*, *Phys. Rev. Lett.* **74**, 3548 (1995).

4.2 C0 Baseline Detector Description

We describe here the baseline detector for BTeV, which can achieve our physics goals, and is designed to have the capability to perform new measurements on new interesting final states that may turn out to be recognized as important in the future.

The challenges for any future hadron collider B experiment are to achieve high efficiency and low background in the hostile and complex environment of a hadron collider. This requires the effective and aggressive use of the most modern technologies. For BTeV this represents a significant step beyond what will be achieved by the upcoming generation of hadron collider B experiments and e^+e^- collider experiments running on the Υ(4S), and their possible extensions and upgrades. Furthermore, we must be able to compete successfully with the LHC-b experiment, when it starts running.

BTeV has begun to take shape based on an understanding of what needs to be done to meet these challenges. These are the key design features of BTeV:

- a dipole located on the IR, which gives BTeV an effective 'two arm' acceptance;
- a precision vertex detector based on planar pixel arrays;
- a vertex trigger at Level 1 which makes BTeV very efficient for many final states, even if they have no leptons in them; and
- excellent particle identification. Especially important is the requirement of very good charged hadron identification. Many of the states that will be of interest in this phase of bottom and charm physics will only be separable from other states if this capability exists. Also, it will allow for the possibility of kaon tagging. Muon and electron identification are important for tagging and for studies of decay modes involving leptons, too.
- A high quality $PbWO_4$ electromagnetic calorimeter capable of detecting final states with single photons, π^o's, η's or η''s.

The parameters of the Tevatron that must be taken into account in creating a design for meeting these challenges are given in Table 4.1. A schematic of the experiment is given in Fig. 4.5. We now discuss the key elements of the baseline design.

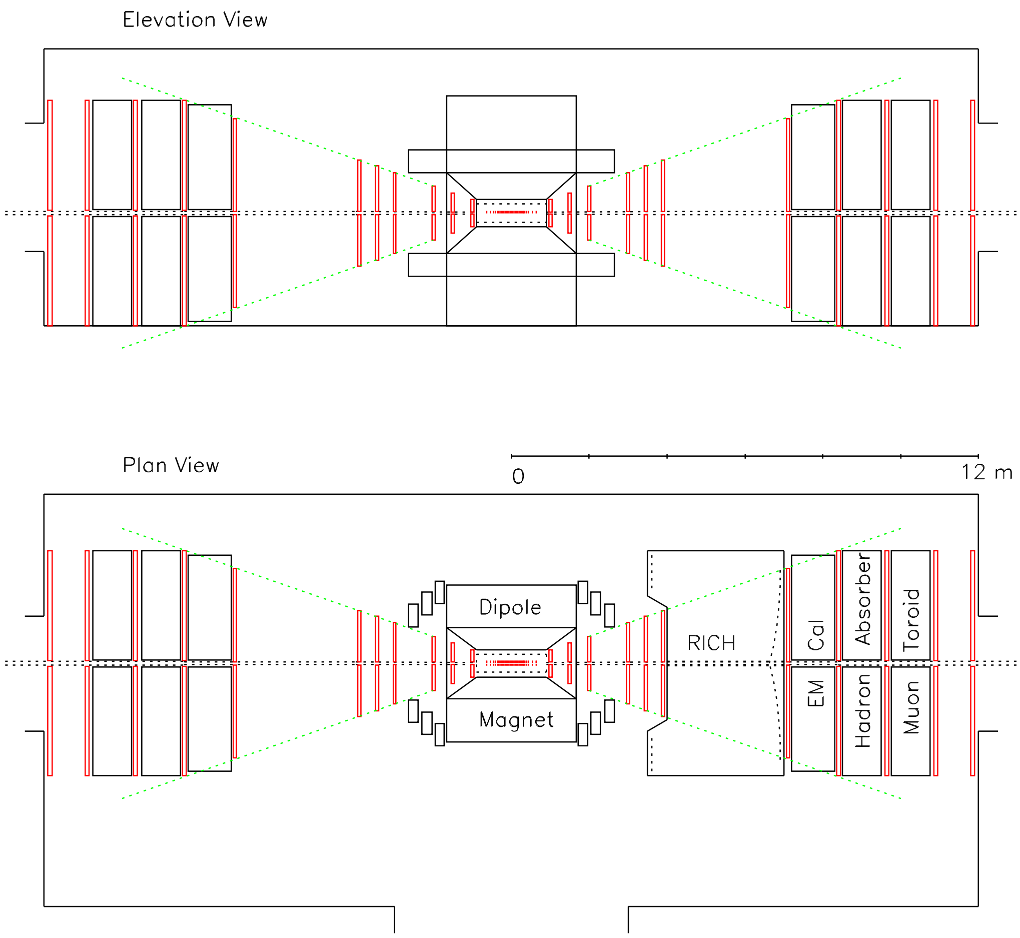

Figure 4.5: Layout of BTeV/C0 Spectrometer

4.2.1 The C0 Experimental Area

The experiment will be carried out in the newly constructed C0 test hall, see Figure 4.6. The test hall is a 216 m^2 (9m wide by 24m long) enclosure centered along the C0 straight section of the Tevatron. (In plan view, the hall is asymmetric transversely, extending 3.5m from the beam on the west side and 5.5m from the beam on the east side.) The Tevatron beam is 2.5m above the floor slab and 4.25m below the roof of the hall. There are flared transition enclosures both upstream and downstream of the test hall. The test hall specifications and dimensions are compatible with the detector described in this document.

To the east of the test hall is the C0 assembly building (see Figure 4.7) a steel framed, industrial type, structure containing a 150m^2 assembly hall at the test hall elevation. Detector components will be constructed in the assembly hall and moved into the test hall through a 6m $\times$ 6m 'shield door'. The C0 assembly building also has space on various levels for the electrical, water and air handling systems needed for the BTeV detector. Figure 4.8 shows a layout of the assembly building and test hall with the magnet and muon toroids of the proposed BTeV detector superimposed.

Detector elements are brought into the area at a ground level loading dock and lowered to the assembly floor using the 30 ton crane which covers the loading dock and assembly hall. There is no crane in the beam enclosure; all detector elements must be designed so they can be constructed or staged in the assembly area and moved through the shielding door into the enclosure. During operation the shielding door is sealed with concrete blocks for radiation protection. The blocks are stored in the south end of the assembly area in an alcove when the door is open.

There are cable ducts from the experiment enclosure to a 150m^2 equipment room at grade level on the north end of the assembly building. Preliminary engineering has been done on converting this equipment room into a two or three level electronics/counting room and office area for experimenters. Electric power, air handling, other utilities, as well as an elevator, lavatories, etc., although not yet installed, have been designed to accommodate BTeV needs in these areas.

Figure 4.6: C0 Test Hall

Figure 4.7: Tevatron berm and C0 Assembly Building

Figure 4.8: Layout of C-0 Test Area

4.2.2 The BTeV/C0 Spectrometer Magnet

We have identified a magnet that satisfies the specifications for the BTeV/C0 spectrometer. The SM3 magnet, currently part of the decommissioned Fermilab MEast spectrometer, is shown on the proposed layout, Fig. 4.5, of the BTeV/C0 spectrometer. This magnet was assembled in 1981 from soft iron blocks recovered from the decommissioned Nevis Cyclotron. The coils for the magnet were built of 5 cm square aluminum conductor by the Sumitomo Corporation under the aegis of the US-Japan Agreement on High Energy Physics. The magnet operated in MEast from 1982 until 1997, at a central field of about 0.8 Tesla, serving experiments E605, E772, E789, and E866.

The SM3 magnet was assembled by welding together, in place, various blocks of steel. It has a total weight of 500 metric tons. The construction and assembly drawings for this magnet have been located. Engineering preparations are now underway for disassembling the magnet. The modified magnet could then be reassembled in the C0 assembly hall and rolled into the C0 collision hall, as shown in Fig. 4.6.

The central field specified for the BTeV/C0 spectrometer is much higher than the past operating excitation of the SM3 magnet. Preliminary studies with magnetostatic modeling programs (POISSON and OPERA) have led to a design for a new pole-piece for SM3. This pole-piece, indicated in Fig. 4.9, yields a central field of 1.6 Tesla, and an integrated dipole field of 5.2 T-m.

The design has an integrated sextupole field component on the symmetry axis of 0.002 T/m. This is small compared to the natural sextupole moment of the Tevatron dipoles and is acceptable for insertion into the Tevatron lattice. In this design the magnet would draw 650 kW of power at 4200 amps, similar to its past operating power level (it was powered by two 500 kW Transrex power supplies). Note that the magnet will be oriented so that charged particles are deflected in the vertical plane. The properties of the magnet, with the pole faces shimmed to the BTeV requirements, are shown in Table 4.2.

Table 4.2: BTeV/C0 Vertex Dipole Properties

Property	Value	Comment
$\int B \times dl$	5.2 T-m	2.6 T-m on each side of center of IR
Central Field	1.6 Tesla	
Steel Length	3.2 m	
Overall length	5.3 m	
Magnet Vert. aperture	± 0.3 rad	
Magnet Horz. aperture	± 0.3 rad	

The magnet is centered on the interaction region in Z thus creating both an ‘upstream’ and ‘downstream’ spectrometer. In quark-antiquark production at 2 TeV, the bottom quark

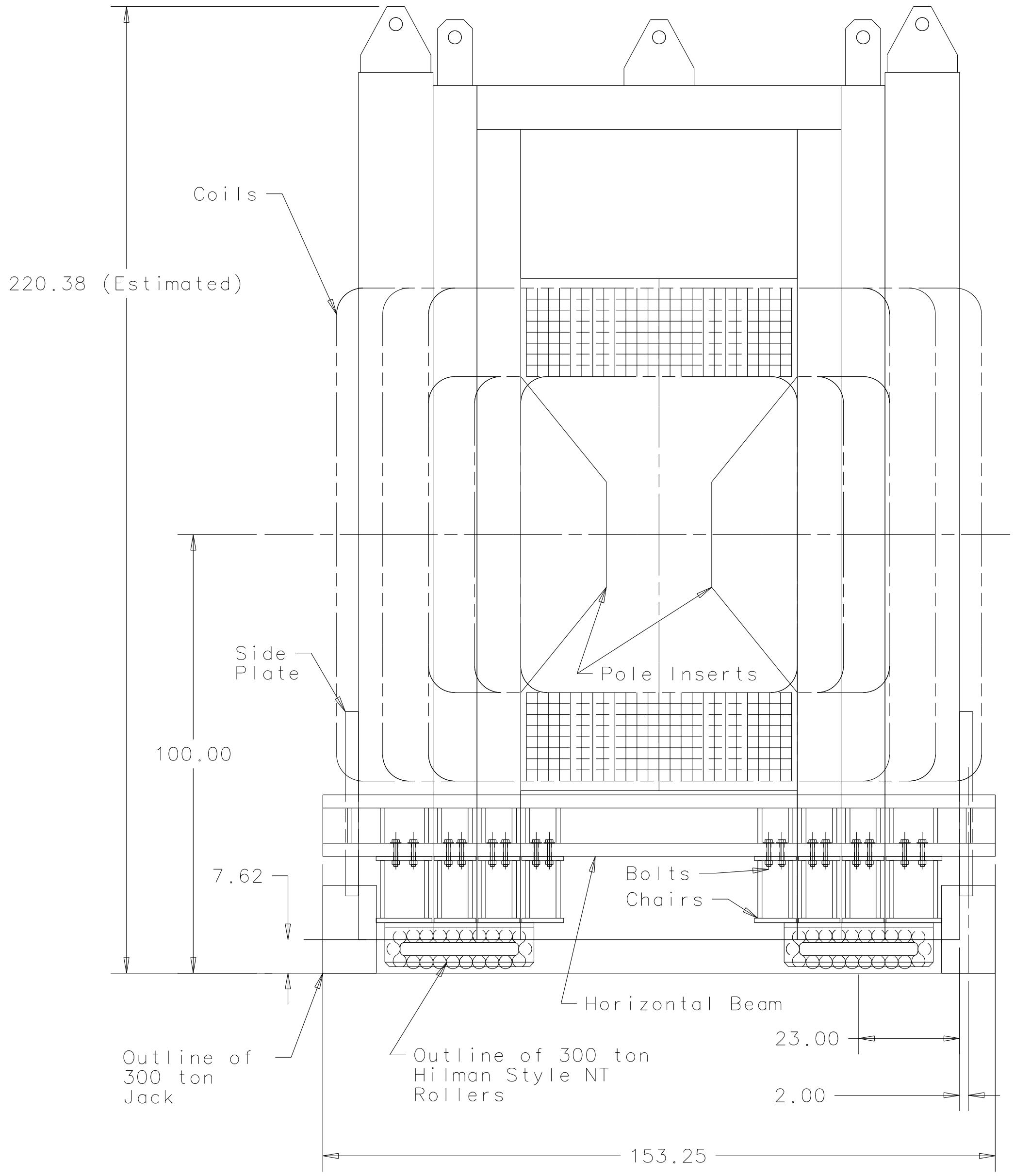

Figure 4.9: Cross section of the modified SM3 dipole with rollers and pole piece inserts. All dimensions are in inches.

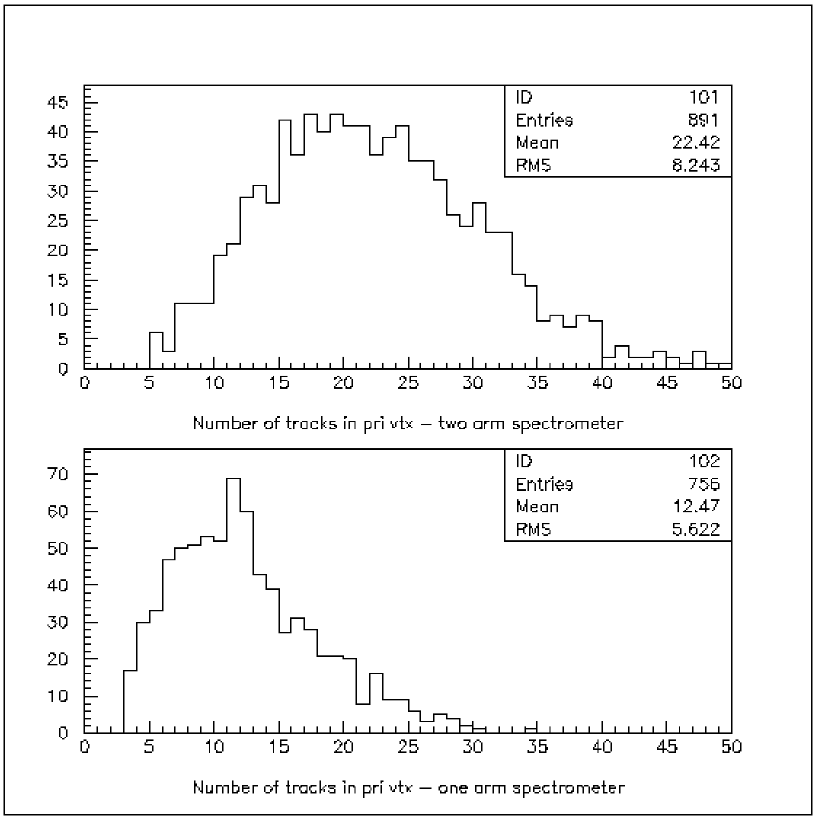

Figure 4.10: Fraction of events with N primary tracks above 1 GeV/c momentum for a) a dipole centered on the IR giving an effective two-arm acceptance and b) a single forward spectrometer arm.

and antiquark are usually either both boosted upstream or both boosted downstream. Thus having two spectrometers doubles the acceptance of the experiment for tagged decays. Having two spectrometers further improves the experiment because the extended coverage increases the number of tracks from the underlying event that can be used to determine the primary vertex. Fig. 4.10 shows the number of high energy primary tracks (low multiple scattering) that contribute to locating the primary vertex for single arm coverage and for two arm coverage. If we require three such tracks to determine the primary vertex, then 2.2 times more events survive with two arms than with one, and the primary vertex resolution is enhanced.

In this central dipole geometry, there is a strong magnetic field at the vertex detector. Because of the excellent spatial resolution of the vertex detector, it is possible to get a crude measurement of the track momentum using the vertex detector alone. This measurement can be used to reject tracks at the trigger level that are at such low momentum that multiple coulomb scattering errors make their assignment to a vertex uncertain.

The second spectrometer arm will also be useful during the R&D and early data-taking phases of the experiment. It is possible, given the lab's budget, that only one arm will be fully instrumented initially. The other side can be used to test new detector concepts or to test prototypes of production components under actual beam conditions until it becomes possible to instrument it fully.

4.2.3 Tracking System

The tracking system is designed to reconstruct tracks and measure their angles and momenta over the full aperture ($\pm$300 mr $\times$ $\pm$ 300 mr) and momentum acceptance (from 1 GeV/c to more than 100 GeV/c) of the experiment. The main requirements that have to be satisfied by the system are:

- Provide adequate resolution on track positions, at least 9μm or better, and angles, at least 0.1 mr, to separate with high efficiency and robustness the secondary vertices of bottom and charm decays from the primary interaction vertex
- Provide sufficient momentum resolution, about 1% at 100 GeV/c, to permit the reconstruction of the invariant mass of multibody bottom and charm decays with good precision
- Deliver its information to a Level 1 trigger processor which implements a trigger based on detached vertices or tracks with large impact parameters
- Handle the rates and tolerate the radiation doses expected in the experiment

To satisfy these requirements, the experiment will employ two tracking subsystems which work together to provide efficient track reconstruction, excellent vertex resolution, and excellent momentum and mass resolution. These are

- The vertex detector which provides the precise vertex measurement and also has momentum measurement capability. The signals from the vertex detector provide the main input to the Level 1 vertex trigger.
- The forward tracker, which provides, along with the vertex detector, precision momentum measurement. It also permits us to reconstruct tracks from K_s^o's and Λ's, which often decay downstream of the vertex detector.

In the following paragraphs, we discuss the design of each of these systems.

4.2.3.1 Vertex Detector

The vertex pixel detector provides the high resolution tracking near the interaction which is required to associate tracks with their proper vertices – primary and secondaries. In designing a vertex tracking system, one must consider the long interaction region (IR) of the Tevatron, which has a σ_z of 30 cm. This forces one to have a rather long vertex detector. In addition, the detector must be placed very close to the interaction region in order to achieve good resolution and acceptance; so radiation damage is an issue. In this experiment, the vertex detector will be used in the Level 1 trigger to select events with secondary vertices. This places special requirements on the detector and its readout.

The baseline BTeV vertex tracking system uses planar arrays of silicon pixel detectors, placed at intervals along the IR and upstream and downstream of it (to catch tracks coming from the end of the IR). Silicon pixel detectors are chosen because of their:

- Superior signal to noise (expected to be better than 100 to 1 for 300μm thick detectors) as compared to other solutions such as silicon strips
- Excellent spatial resolution. This includes the ability to improve the spatial resolution by measuring the charge sharing between adjacent pixels
- Low occupancy due to the large number of channels
- Intrinsically better pattern recognition capabilities compared to strip detectors
- Speed of response
- Radiation hardness

It is especially important for the trigger that the number of spurious noise hits be as low as possible. Also, the vertex tracking system must not produce pattern recognition ambiguities or ghost tracks which would take extra time to sort out at the trigger level. The two dimensional nature of the pixels is an enormous help in this regard.

The baseline vertex detector, shown in Fig. 4.11, has rectangular 50μm by 400μm pixel detectors. It has triplets of planes distributed along the IR separated by 3.2 cm. The individual planes cover $\pm 5\ cm$ in both transverse dimensions. Acceptance studies show that this is an adequate size for these detectors. They are mounted above and below the beam, and are arranged so that a small square hole of $\pm$6mm $\times$ $\pm$6mm is left for the beams to pass through.

Each triplet consists of one plane that measures the bend view, one that measures the non-bend view, and a third that measures the bend view again. The reason for this particular arrangement of pixel orientations is related to the trigger and is discussed below in the trigger section. A crude momentum measurement can be made using only information from three or four triplets. If the pulse height is read out and made available to the trigger, charge sharing can be used to improve the momentum resolution (the point resolution is expected to be between 5μm and 9μm). The momentum information can be used to reject very soft tracks that would adversely affect the trigger algorithm, and to properly assign multiple coulomb scattering weights to tracks in the vertex fits.

The implementation of this system will be very challenging. Because pixel information must be made available to the first-level trigger, a custom electronic design is necessary. There are also significant mechanical (e.g. alignment and support) and thermal issues that must be addressed. The detector must be shielded electronically from the circulating beam which is a significant rf source. It will be enclosed in a secondary vacuum, isolated from the main accelerator vacuum, by a thin aluminum vacuum container. The silicon should be as close to the beam as possible. A hole of $\pm$6mm on a side will result in the innermost edge of the detector receiving a fluence of close to 2.0×10^{14} per year (10^7 sec) at a luminosity of $2 \times 10^{32}\ cm^{-2} sec^{-1}$. The detector needs to be retractable to a distance of 2 cm from the beam while the collider is being filled and until acceleration is complete. Table 4.3 summarizes the properties of the pixel detector.

While pixel detectors have been successfully operated in HEP experiments, no pixel detector of the proposed size which operates at the high rates we will experience in BTeV, and which can provide signals to the first-level trigger has yet been built. A substantial R&D effort is required to meet the BTeV specifications. Although the BTeV pixel detector is unique, pixel detectors are necessary for several other experiments, and we are taking advantage of work being done all over the world. A status report on the R&D to develop this detector is given in Chapter 5.

We recognize that the design presented here is very challenging. We are studying ways of reducing the technical requirements while incurring only minimal loss of physics reach. We are also particularly interested in reducing the amount of material in the pixel detector in order to reduce the number of conversions of photons from B decays. This is discussed in the chapter on the electromagnetic calorimeter below.

4.2.3.2 Forward tracking system

The purpose of the forward tracking system is to:

- Provide high precision momentum measurements for charged tracks. The vertex detector will provide precise position and direction measurements, but it is too short and contains too much material to provide precise momentum measurements.

- Provide the only trajectory measurements for important classes of tracks which do not pass through the vertex detector. The most important such class consists of K_s's and Λ's which decay downstream of the pixel planes. K_s's are daughter particles in some of the most important bottom and charm decays.

- Confirm and locate tracks at the entrance (and exit) of the RICH, the EM calorimeter, and the muon system. In particular, this system allows one to flag charged tracks that interacted or decayed within the spectrometer volume.

The baseline technology for most of the forward tracker is planes of 4mm diameter straw tubes. Seven stations of tubes are distributed along each arm of the spectrometer. Three of these stations are located in the fringe field of the dipole magnet. Three more are placed between the end of the magnet coils and the RICH entrance window (these establish the direction of tracks entering the RICH). The final plane is located between the RICH and the EM calorimeter. A single station has three sets of straws directed along the three views: Y, U, and V (U and V are at $\pm 45^o$ from Y). Each set in a station is made up of three layers of parallel straws.

The straw tube chambers are expected to provide a spatial resolution of $\sim 150\mu$m per plane. Three parallel straw tubes per station will yield a resolution of better than 100μm in each of the three views. This resolution is sufficient to provide a momentum resolution between 0.5% and 1% for momenta between 1 GeV/c and 100 GeV/c.

Recent simulations have demonstrated that at a luminosity of $2 \times 10^{32}\ cm^{-2} sec^{-1}$, 4mm diameter straw tubes do not provide adequate segmentation near the beamline in the first three measuring stations. As is discussed in Chapter 6, we have modified the baseline design to include silicon strip detectors to cover the central portion of these stations.

Tables 4.4 and 4.5 summarize the baseline design specifications for the straw tube and silicon strip subsystems of the forward tracker.

4.2.3.3 Diamond Pixel Option

Diamond pixel detectors could have significant advantages over silicon pixel detectors but are in an earlier stage of development. The recombination length of diamond has improved steadily in the last couple of years and is now around 150 μm. The resulting signal is about a factor of three lower than that of silicon. Research on improving the signal collection continues. Properties of diamond that make it superior to silicon if sufficient pulse height can be obtained are:

- lower radiation length leading to lower multiple scattering;
- better radiation hardness; and
- better thermal conductivity which leads to simpler cooling schemes which can result in less material in the detector.

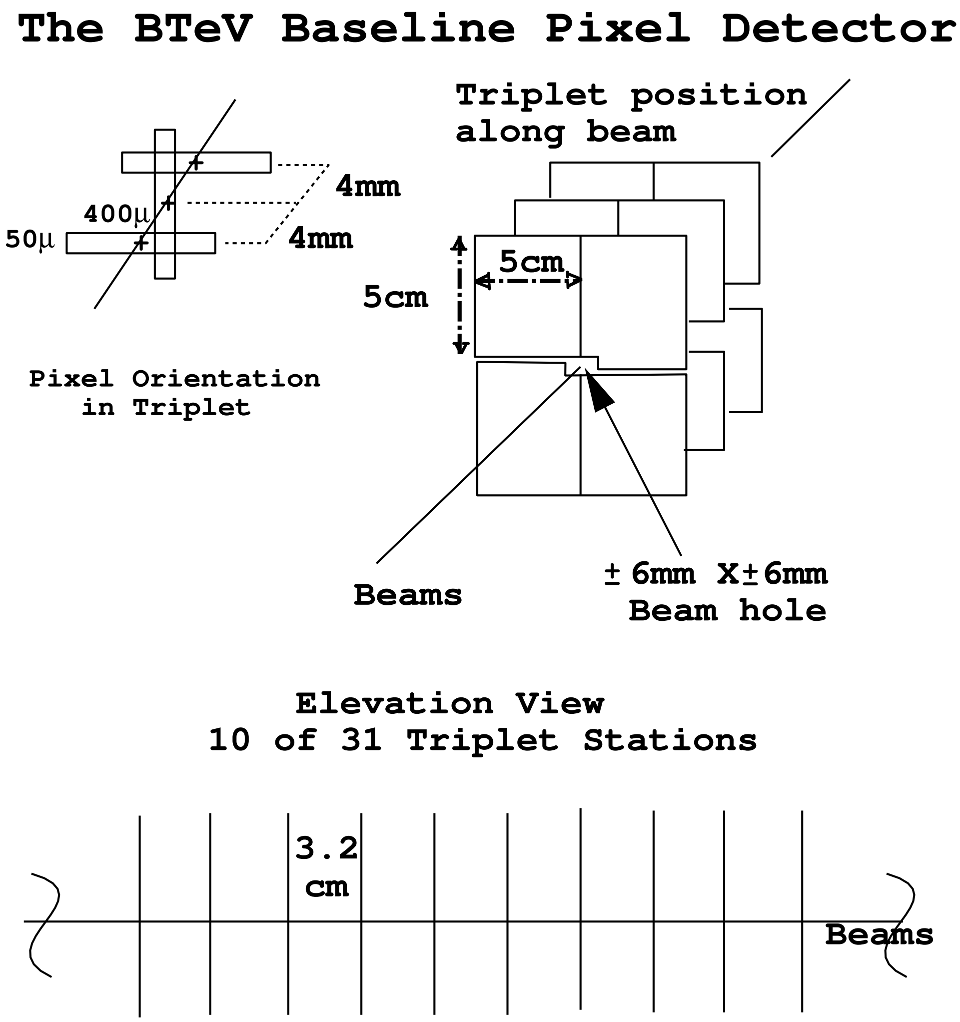

Figure 4.11: Baseline pixel vertex detector

Table 4.3: Properties of Baseline Pixel Vertex Detector

Property	Value
Pixel size	rectangular: 50μm $\times$ 400μm
Plane Dimensions– upper half	10cm $\times$ 5cm
Plane Dimensions– lower half	10cm $\times$ 5cm
Central square hole (adjustable)	nominal setting: 12x12mm
Total Planes	93
Total Stations	31, each consisting of three planes
Pixel orientations	the outer two with narrow pixel dimension vertical the middle one with narrow pixel dimension horizontal
Separation of Stations	3.2 cm
Plane to plane separation (within station)	4 mm
Total Plane Thickness (incl cooling, supports)	1000 μm Si equivalent
Station Thickness (incl. Al shielding skin)	3200 μm Si equivalent
Total Pixels	4.2×10^7
Total Silicon Area	$\approx$1m^2
Readout	analog readout (no. of bits to be decided)
Trigger	signals are used in Level 1 trigger
Rate requirements	beam crossing rate is 132 ns.
Deadtime	<3% at 2×10^{32}cm^{-2}s^{-1}
Noise requirement	desired: $< 10^{-6}$ per channel per crossing required: $< 10^{-5}$ per channel per crossing
Resolution	9μm or better
Alignment accuracy	5μm or better
Radiation tolerance	$\approx 6 \times 10^{14}$ particles/cm^2
Power per pixel	<40 μWatt

Table 4.4: Properties of the baseline forward straw tracker

Property	Value
Straw size	4mm diameter
Central hole	5 cm $\times$ 5 cm to 24 cm $\times$ 24 cm
Total Stations	14 (7 per arm)
Z positions (cm)	96, 146, 196, 296, 341, 386, 706
Half size (cm)	30, 45, 60, 90, 105, 118, 210
Views per station	3
Layers per view	3
Total number of straws	78132
Total station thickness ($< L > /X_0$)	0.6%
Readout	ASD + timing chip (6 bits), sparsified
Total channels	118,464
Rate requirements	beam crossing rate is 132 ns.

Table 4.5: Properties of the proposed baseline forward silicon tracker

Property	Value
Wafers	4×6 cm^2 / 2.5×4.75 cm^2
Pitch	100 μm
Thickness	300 μm
Ladder modules	12 per station
Coverage	24 cm $\times$ 24 cm
Central hole	5 cm $\times$ 5 cm
Total stations	6 (3 per arm)
Z positions (cm)	100, 150, 200
Measurement views	4 (X,Y,U,V)
Channels per view	2400
Total channels	57600
Readout	double-sided, sparsified binary

4.2.4 Triggering System

The proposed broad charm and beauty physics program of BTeV/C0 calls for a trigger whose efficiency

- is large for heavy-quark decay events which can be found off-line and
- is relatively independent of decay mode.

Because the program has many goals and will undergo several phases of development, the trigger needs to be flexible. We plan to implement a multi-level trigger with several "branches" that can be independently prescaled and then combined into a global trigger. These will include muon and dimuon triggers, general interaction triggers, and possibly electron and dielectron triggers. However, the demands of a collider B experiment are difficult to meet with simple, conventional approaches to triggering. In particular, the second criterion above is not satisfied by simple triggers commonly used in hadron collider experiments, e.g. lepton triggers. BTeV's main B-physics trigger focuses on the key difference between heavy quark events and typical hadronic events – the presence of detached vertices – at the first trigger level, Level 1. It is very efficient for the B decays that can be successfully reconstructed by the spectrometer. It also avoids the need to focus at Level 1 on specific final states, which can limit the accessible physics. Its implementation requires a very sophisticated trigger architecture which also provides a more than adequate foundation for any of the other triggers we are considering.

In this section, we focus on the Level 1 detached vertex trigger, for which we are carrying out a program of research and development, based on extensive simulation and design studies. Details some of the other triggers – the muon trigger and the electron trigger – are given in the sections on the muon detector and the electromagnetic calorimeter.

4.2.4.1 Level 1 Detached Vertex Trigger

The trigger algorithm has the goal to reconstruct tracks and find vertices in every interaction up to an interaction rate of order 15 MHz (luminosity of $2 \times 10^{32}\,\mathrm{cm}^{-2}\,\mathrm{s}^{-1}$ at $\sqrt{s} = 2\,\mathrm{TeV}$). This entails an enormous data rate coming from the detector ($\sim 100\,\mathrm{GB/s}$), thus a careful organization of the data-flow is crucial. This trigger must be able to operate both in collider and fixed-target modes. It must be capable of reducing the trigger rate by a factor of at least 100.

The key ingredients for such a trigger are

1. a vertex detector with excellent spatial resolution, fast readout, and low occupancy;
2. a heavily pipelined and parallel processing architecture well suited to tracking and vertex finding;
3. inexpensive processing nodes, optimized for specific tasks within the overall architecture;

4. sufficient memory to buffer the event data while the calculations are carried out; and

5. a switching and control network to orchestrate the data movement through the system.

The pixel detector described above is the first ingredient. Use of pixels for the tracker will produce very high spatial resolution for the trigger (and the final analysis) and, because of their 2-dimensional nature and excellent signal-to-noise, will reduce the level of potential confusion during the crucial track-finding phase of the trigger. Since the pixel detector is located in a magnetic field, some momentum information can be derived from the bending in the pixel detector alone without needing to use the downstream tracking system. If, in addition, the pixels have pulse height readout, they can achieve a spatial resolution of less than 12 μm, which provides rather good momentum information to the Level 1 trigger.

To provide the second ingredient, we employ parallelism both at the subevent level and at the event level. The detector layout described above has "stations" consisting of three planes. Processors organize the hits in each triplet of planes into "station hits". Still at the subevent level, individual processors work on the station hits from a slice of the detector, as will be described below. At the event level, track candidates from the individual slices are brought together in a common processing node, one member of a large farm, for vertex finding.

The third ingredient is provided by using large numbers of inexpensive, commercially available CPU chips. New processors are constantly appearing on the market, often optimized for very specific tasks, and prices are dropping rapidly. Research is in progress to determine the characteristics of the processors needed at each stage.

The fourth ingredient is also commercially available. The time allowed to process the data is limited by the number of events which can be stored while the trigger decision is being made. An event is expected to be significantly less than 200,000 bytes. The memory required to buffer 256 crossings even for 200,000 byte events is only 50 MB and is adequate for a decision time of 33 μs. This system can be off the detector (i.e. not in a strong radiation environment) so commercial (PC) memories are adequate and the costs are small on the scale of the full trigger system. Memory costs do not limit the decision time which could be much longer if necessary.

The final ingredient is switching networks which appear at the input of each section of the Level I trigger and between the Level 1 trigger and next level of triggering. The design of this switching hardware is under study.

The reference trigger scheme was originally developed by the Penn Group - Selove, Sterner, and Isik [4]. While it has undergone major revisions and is still being updated, it has been an excellent starting point for studying this kind of trigger.

The proposed algorithm has four steps:

1. In the first step, hits from each pixel plane are assigned to detector subunits. This can be done very rapidly for all planes in parallel using field-programmable gate arrays (FPGAs). It is desirable to subdivide the area of the detectors in a way which minimizes the number of tracks crossing from one subunit into the next and assures uniform and

low occupancy (< 1 hit/event) in all subunits. We therefore divide each plane into 32 azimuthal sectors ("ϕ-slices"). Simulation shows that at 2 TeV, on average each ϕ-slice contains 0.3 hits per inelastic interaction, approximately independent of the plane's z coordinate.

2. In the second step, "station hits" are formed in each triplet of closely-spaced planes using hits from each ϕ-slice. Since the pixels under consideration have a rectangular shape (e.g. $50\,\mu$m by $400\,\mu$m), the two outer planes in each station are oriented for best resolution in the bend view, and the inner plane for the non-bend view. There is a "hit processor" for each ϕ-slice of each station. The hit processor finds triplets of overlapping pixels, and sends to the next stage a single "minivector" consisting of x, y, $\frac{dx}{dz}$ and $\frac{dy}{dz}$. Given the good position resolution of each measurement, a detector station determines a space point accurate to $5-9\,\mu$m in x and y, and y and x slopes to $\frac{dy}{dz} \approx 1\,$mr (bend-view) and $\frac{dx}{dz} \approx 10\,$mr (non-bend). The use of these minivectors in the track-finding stage substantially reduces combinatorics.

3. In the third step, minivectors in each ϕ-slice from the full set of stations are passed via a sorting switch to a farm of "track processors." The sign of the bend-view slope is used to distinguish forward-going and backward-going minivectors and send them to separate farms. To handle the few percent of tracks crossing segment boundaries, hits near a boundary between two ϕ-slices can be sent to the processors for both slices.

   Each track processor links minivectors into tracks, proceeding along z from station to station. For each pair of minivectors in adjacent stations, the processor averages the y-slopes in the two stations and uses this average slope (which represents the slope of the chord of the magnetically deflected trajectory) to project from the first station into the second. It then checks whether the y-value of the minivector in the downstream station agrees with the projection within an acceptance window. If three or more hits satisfy this requirement, a fast fitting algorithm finds the momentum of the track candidate.

4. In the fourth step, the tracks are passed to a farm of "vertex processors" and used to form vertices. The vertex with $\sum p_z$ closest to zero is designated as the primary vertex. Tracks which have a large impact parameter with respect to this vertex are taken as evidence for heavy quark production in an event. To reduce the effect of multiple scattering on vertex resolution, tracks below an adjustable bend-view transverse-momentum (p_y) threshold are excluded from the vertex finding.

It is desirable to have pulse-height information included with each hit so that interpolation can be used to improve the point resolution beyond the $50\,\mu\text{m}/\sqrt{12}$ otherwise available. Digital (1 bit) readout seems to be adequate for the p_y cut, but the improved momentum resolution with analog information would allow the processor to calculate the mass of the charged particles at a vertex, which may be a useful variable on which to cut if additional rejection is needed. It also can improve the position accuracy for tracks incident at large angles, which cross over rows or columns of pixels.

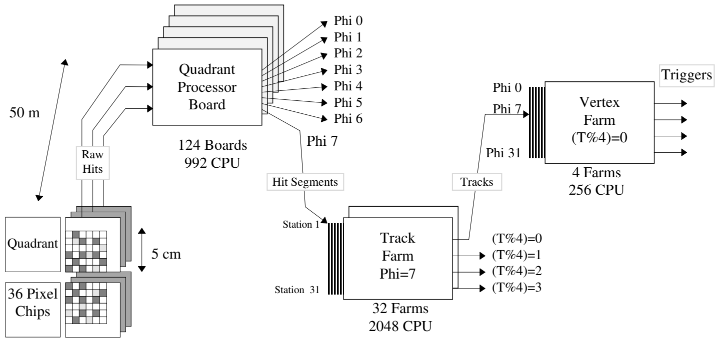

Figure 4.12: Schematic of Proposed Level 1 vertex trigger

The Level 1 rejection factor for events containing only light quarks is required to be approximately 10^{-2} in order to reduce the data rate into Level 2 to sufficiently low levels. The overall acceptance for $B \to \pi^+\pi^-$ events is expected to be 10-20% for the proposed BTeV Level 1 vertex trigger. The expected trigger efficiency for $B \to \pi^+\pi^-$ events that will have both B daughter πs reconstructed should be much higher – about 50%. Results of simulation studies with this trigger will be described below in Chapter 8.

D. Husby and W. Selove have developed a detailed proposal for this trigger system. In this design there are about 1000 hit processors, 2000 track processors, and 128 vertex processors. Since the architecture is scalable, there is flexibility for these numbers to be optimized to meet unanticipated conditions. The design uses a combination of digital signal processors (DSPs), FPGAs and commercial CPUs. Fig. 4.12 shows a schematic diagram of the full system. Details of their current design can be found in Ref. [5]. A hardware design has been worked out for a small-scale prototype; see the trigger research and development section for details.

4.2.4.2 Development of other Level 1 triggers and the global trigger framework

While we have emphasized the "vertex/impact parameter" trigger because it is our most crucial and most ambitious trigger, we will also have other triggers at Level 1. These will include muon and electron triggers and perhaps some triggers derived from the same hardware that is used for the vertex trigger but optimized for different physics. At the output of the first level trigger there will be a 'global Level 1 trigger' subsystem that will allow us to combine the various individual trigger elements into final triggers (for example, an event with only weak evidence for a secondary vertex but with an indication of a high p_t single lepton might be accepted). It will also have the ability to apply a programmable prescale to the various triggers before the are 'or'ed together to form the final trigger. We will probably also include the ability to dynamically change the prescales during the course of the store.

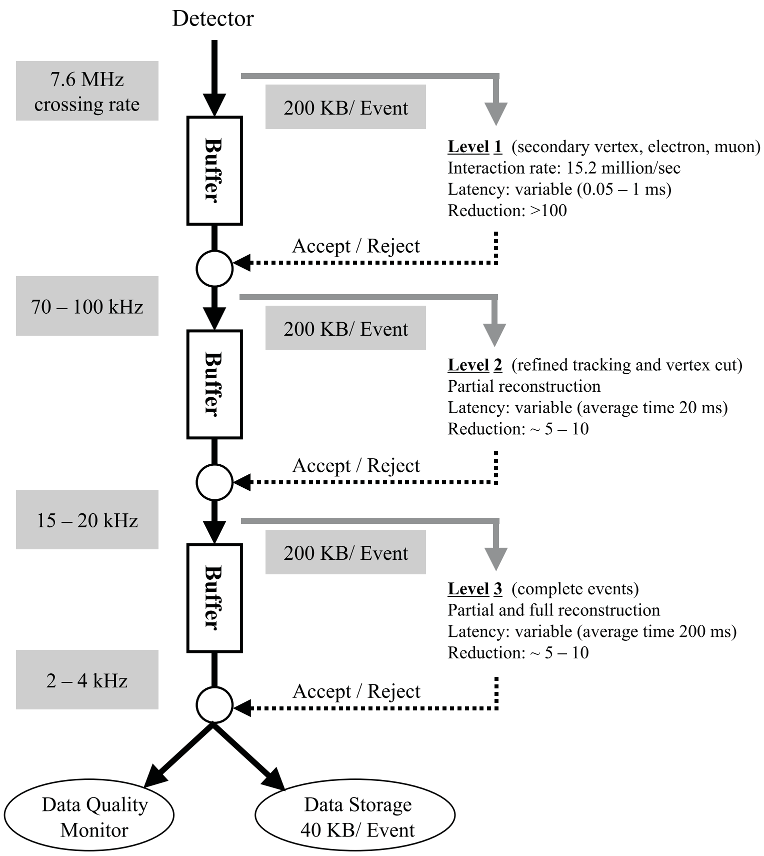

Figure 4.13: The BTeV data flow diagram. The numbers are for the nominal luminosity of $2 \times 10^{32}\mathrm{cm}^{-2}\mathrm{s}^{-1}$.

4.2.4.3 Beyond the Level 1 Trigger

Modern experiments in high energy physics implement hierarchical trigger systems and BTeV is no exception. Many details of the full data acquisition system have to be worked out as the design of the detector components and trigger algorithms become more mature. At the design luminosity of $2 \times 10^{32}\mathrm{cm}^{-2}\mathrm{s}^{-1}$ and with a total inelastic cross section of $\sigma_{inel} \approx 60$mb almost every crossing will have an interaction, so events will have to be examined at the crossing rate of 7.5 MHz. Fig. 4.13 gives the outline of the expected data flow at the nominal design luminosity.

At our current level of understanding, the needed level 1 rejection factor seems to be achievable even if the only test made is for a detached vertex in vacuum. The event rate is then reduced to ≈100 kHz in the worst case during the highest luminosity running. It is still possible to move all this data, amounting to a maximum rate of 10 GB/s, to the Level 2 trigger.

Events that pass the first trigger level are forwarded to compute nodes to be further analyzed. First, information from other detectors besides the pixel detector is used to get better values of the momentum of the tracks. The vertex detachment requirement is then imposed with a better knowledge of the error matrices of the tracks and improved vertex assignments are computed. Events remaining after this step are then fully assembled in a switch-based event builder and passed to a processor farm. Even so, it will probably be impractical to write several kHz of events to archival storage.

The final trigger level will combine information from different sub-detectors to further suppress background events. Particle identification will be available at this stage and could be used to obtain a very clean direct charm signal for specific final states. We intend to fully reconstruct the events at this level before the data are sent to a storage system and made available for off-line processing.

Because the event rate surviving this last level may still be close a few kHz, the software will probably have to reduce the amount of data per event to archival storage by writing out an event summary which eliminates much of the raw data. The event summary would be around 50 KB so that the output rate could still be as high as 80 MB/s. This results in a dataset size of 800 TB/yr, somewhat more than is expected from CDF or D0 in Run II. However, initial phases of the experiment will run at much lower rates and will be comparable in dataset size to a current fixed target experiment.

4.2.4.4 Additional Work

Although simulation results are very encouraging, much additional simulation work and a vigorous R&D program are needed to implement such a triggering system. The simulation work involves studying the performance of these proposed Level 1 and Level 2 algorithms under realistic experimental conditions, which include detector inefficiencies, photon conversions, delta ray production, hadronic interactions in the silicon, low energy loopers, multiple interactions, electronic noise, machine backgrounds, and beam-induced backgrounds (e.g. scraping in the support structures and/or beam pipe). Some of these studies have already been done and are presented in Chapter 8.

4.2.5 Particle Identification

Excellent charged hadron particle identification is a critical component of a heavy quark experiment. Even for a spectrometer with the excellent mass resolution of BTeV, there are kinematic regions where signals from one final state will overlap those of another final state. For example, $B_d^o \rightarrow \pi^+\pi^-$, $B_d^o \rightarrow K^+\pi^-$, and $B_s^o \rightarrow K^+K^-$ all overlap to some degree leading to ambiguous classification of the final state. These ambiguities can be eliminated almost entirely by an effective particle identifier. In addition, many physics investigations involving neutral B-mesons require 'tagging' of the flavor of the signal particle by examining the properties of the 'away-side' particle. Our studies show that kaon tagging is a very effective means of doing this.

4.2.5.1 Requirements

In the design of any particle identification system, the dominant consideration is the momentum range over which efficient separation of the various charged hadron types – π, K, and p – must be provided. In BTeV, the physics goal which sets the upper end of the momentum requirement is the desire to cleanly separate $B_d^o \rightarrow \pi^+\pi^-$ from $B_d^o \rightarrow K^+\pi^-$ and $B_s^o \rightarrow K^+K^-$. These two-body decays produce reasonably high momentum pions and kaons. Fig. 4.14 shows the momentum distribution of pions from the decay $B_d^o \rightarrow \pi^+\pi^-$ mentioned above for the case where the two particles are within the spectrometer's acceptance. The low momentum requirement is defined by having high efficiency for 'tagging' kaons from generic B decays. Since these kaons come mainly from daughter D-mesons in multibody final state B-decays, they typically have much lower momentum than the particles in two body decays. Fig. 4.15 shows the momentum distribution of 'tagging' kaons for the case where the signal particles are within the geometric acceptance of the spectrometer. About 1/5 of the tagging kaons never exit the end of the spectrometer dipole. Almost all kaons exiting the dipole have momenta above 3 GeV. Based on these plots, we have set the momentum range requirement for the particle identification system to be

$$3\,\mathrm{GeV/c} \;<\; P_{particle\ id} \;<\sim 70\,\mathrm{GeV/c} \tag{4.2}$$

Finally, kaons and pions from directly produced charm decays have momenta which are not very different from the kaons from B-decays. Fig. 4.16 shows the momentum spectra of kaons from accepted $D^o \rightarrow K^-\pi^+$, $D^o \rightarrow K^-\pi^+\pi^-\pi^+$, and $D_s^+ \rightarrow K^+K^-\pi^+$ in both collider and fixed target mode. The range set by the B-physics requirements is a reasonable, if not optimal, choice also for charm physics.

4.2.5.2 RICH radiators

Because of the large momentum range and limited longitudinal space available for a particle identification system in the C0 enclosure, there is really only one choice of detector technology – a gaseous ring-imaging Cherenkov counter. Pions and kaons can be separated in this momentum region with a single gas radiator like C_4F_{10} ($n = 1.00138$ in visible range). Some

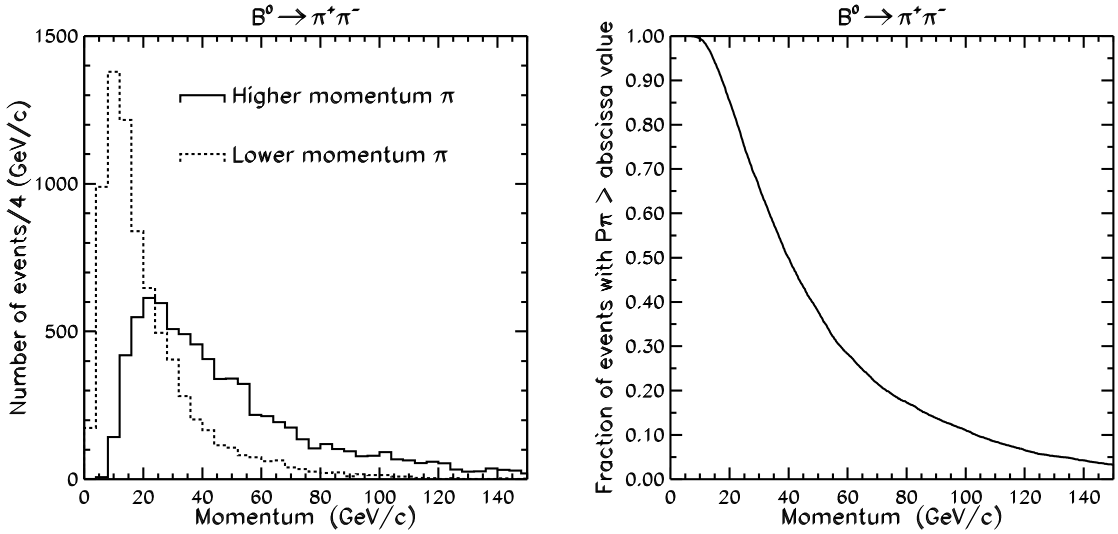

Figure 4.14: The momentum distribution of pions in $B_d \to \pi^+\pi^-$ decays. The left plot shows distributions for the lower (dashed line) and higher (solid line) momentum pion in this decay. The right plot presents the latter distribution in integral form, which gives loss of efficiency as a function of the high momentum cut-off of the particle ID device.

Parameter	C_4F_{10}	aerogel
n	1.00138	1.03
$\Theta_c(\beta$=1)	52.5 mrad	243 mrad
π threshold	2.5 GeV/c	0.6 GeV/c
K threshold	9.0 GeV/c	2.0 GeV/c
p threshold	17.1 GeV/c	3.8 GeV/c
thickness	283cm	5cm

Table 4.6: Several parameters for the proposed gaseous and solid radiators.

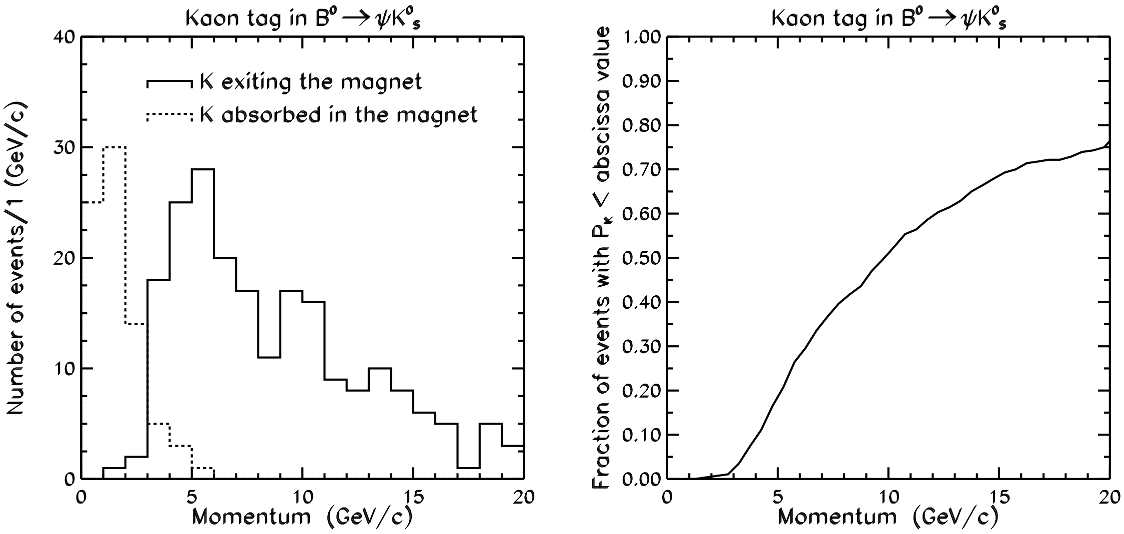

Figure 4.15: The momentum distribution of 'tagging' kaons for the case where the signal particles (ψK_S^0) are within the geometric acceptance of the spectrometer. The left plot shows distributions for kaons absorbed in (dashed line) and exiting from (solid line) the magnet. The right plot presents the latter distribution in integral form, which gives loss of efficiency as a function of the low momentum cut-off of the particle ID device.

parameters of this gas are given in Table 4.6. Among other experiments, C_4F_{10} is used in DELPHI (endcap) [1], HERA-B [2] and HERMES RICH detectors [3]. It was also chosen for one of the LHC-B RICH detectors [4].

Note that below about 9 GeV, no gas can provide K/p separation and that, since kaons are below threshold, the RICH operates in a threshold mode (except that it has much better noise discrimination than a normal threshold counter because it still measures a Cherenkov ring for pions). In order to improve identification of low momentum particles, one interesting possibility is to insert a thin ($\sim$ 5 cm) piece of aerogel at the entrance to the gas RICH as proposed by LHC-B [5] and already implemented by HERMES [3]. For example, aerogel with a refractive index of $n = 1.03$ would lower the π, K, p momentum thresholds to 0.6, 2.0, 3.8 GeV/c respectively as illustrated in Fig. 4.17. Shorter wavelength Cherenkov photons undergo Raleigh scattering inside the aerogel itself. They are absorbed in the radiator or exit at random angles. A thin window between the aerogel and the gas radiator passes photons only in the visible range, diminishing the scattered component.

The same photo-detection system can detect Cherenkov rings produced in both the gaseous and the aerogel radiators if it operates in visible wavelengths.

4.2.5.3 RICH dimensions

The RICH detector can be located behind the tracking chambers just outside the central dipole magnet, about 4 meters away from the interaction point. The length of the RICH

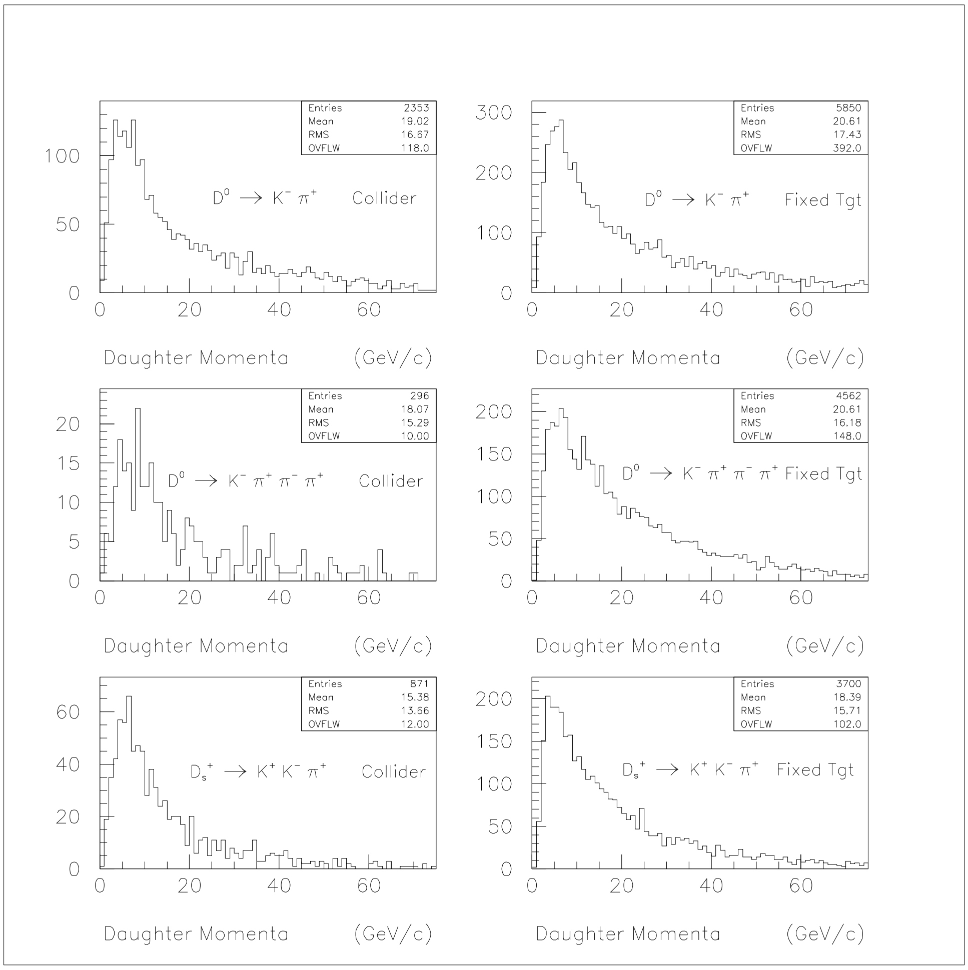

Figure 4.16: The momentum spectra of kaons from accepted $D^o \rightarrow K^-\pi^+$, $D^o \rightarrow K^-\pi^+\pi^-\pi^+$, and $D_s^+ \rightarrow K^+K^-\pi^+$ in both collider and fixed target modes.

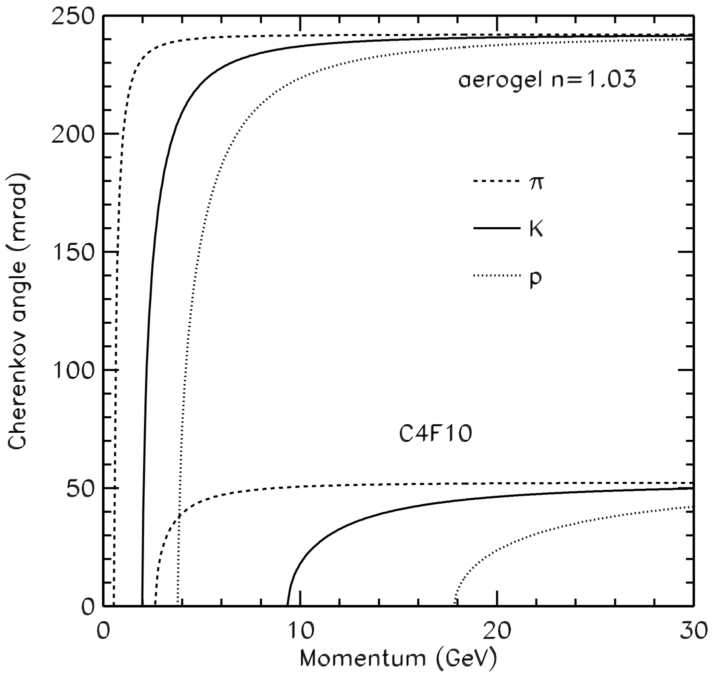

Figure 4.17: Cherenkov angles for various particle species as a function of particle momentum for C_4F_{10} and aerogel ($n = 1.03$) radiators.

detector must be less than 3 meters to allow sufficient space for the EM calorimeter and the muon system. The aerogel radiator with thickness of about 5cm will be mounted at the entrance to the RICH vessel. The gaseous C_4F_{10} radiator will fill the rest of the RICH volume. The transverse dimensions of the RICH entrance window are set by the aperture of the dipole magnet to be about $1.35m \times 1.35m$.

Spherical mirrors at the end of the gas volume reflect Cherenkov photons back and focus them into rings at the photo-detection surface. The photo-detectors should be located away from the flux of particles exiting the magnet, therefore the mirrors are tilted. In order to minimize geometric aberrations from an off-axis mirror configuration, the mirrors will be split along the mid-line of the detector, reflecting photons to photo-detectors located on each side of the vessel in the non-bend view ($x - z$ plane). The longer the RICH detector the smaller the tilt angle. Since the geometric aberrations due to the mirror tilt are significant for the gas radiator, we plan on the longest RICH detector we can accommodate within the space limitations. This also maximizes the photon yield from the gaseous radiator, again improving the resolution of the device. Thus, the gas radiator will be approximately 3 meters long and the mirror radius will be 7 meters. The mirror tilt angle will be about 240 mrads. Note that the mirror tilt angle cannot be further reduced by use of additional flat mirrors at the other end of the detector, like in the designs of HERA-B and downstream LHC-B RICH detectors, since the front of the gas volume must stay transparent to the aerogel photons. The transverse size of the mirror will be about $4m \times 4m$ A possible configuration for the mirrors is to make them from an array of individual hexagons as shown in Fig. 4.18. Each mirror half would consist of 18 full hexagons (76.2 cm tip-to-tip) and 6 half hexagons. A reflectance efficiency over 85% at all relevant wavelengths has been achieved in HERA-B detector with 7mm thick pyrex coated with 200nm Al and 30nm MgF_2.

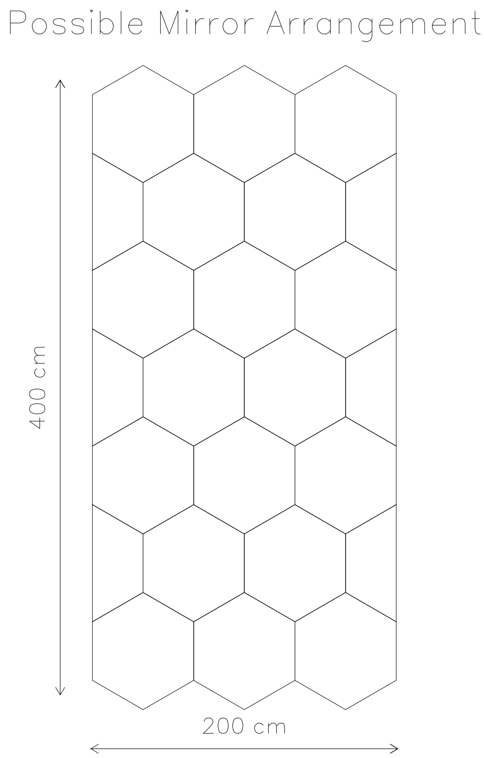

Figure 4.18: Possible arrangement for each half of the mirror using hexagonal mirrors of size 76.2 cm tip-to-tip.

To find the size and optimal position and orientation of the photo-detection surface, we have used a ray tracing Monte Carlo. Even though the true focal plane of a spherical mirror is not planar, non-planar surfaces do not improve resolution significantly and are difficult to realize in practice. Thus, we have assumed that the Cherenkov rings are focused on a plane. We then minimized emission point error for the gaseous radiator with respect to the location of the plane and its orientation using a sample of $B_d \to \pi^+\pi^-$ events. The untilted orientation of the photo-detectors is very close to the optimum. The corresponding contribution to the Cherenkov angle resolution for the gaseous radiator is 0.4 mrad per photon, compared to 0.2 mrad for untilted mirror. As expected for spherical mirrors the photo-detectors must be located about half way between the interaction point and the mirror, which puts them slightly behind the RICH entrance window.

Geometry of the proposed RICH detector is shown in Fig. 4.19.

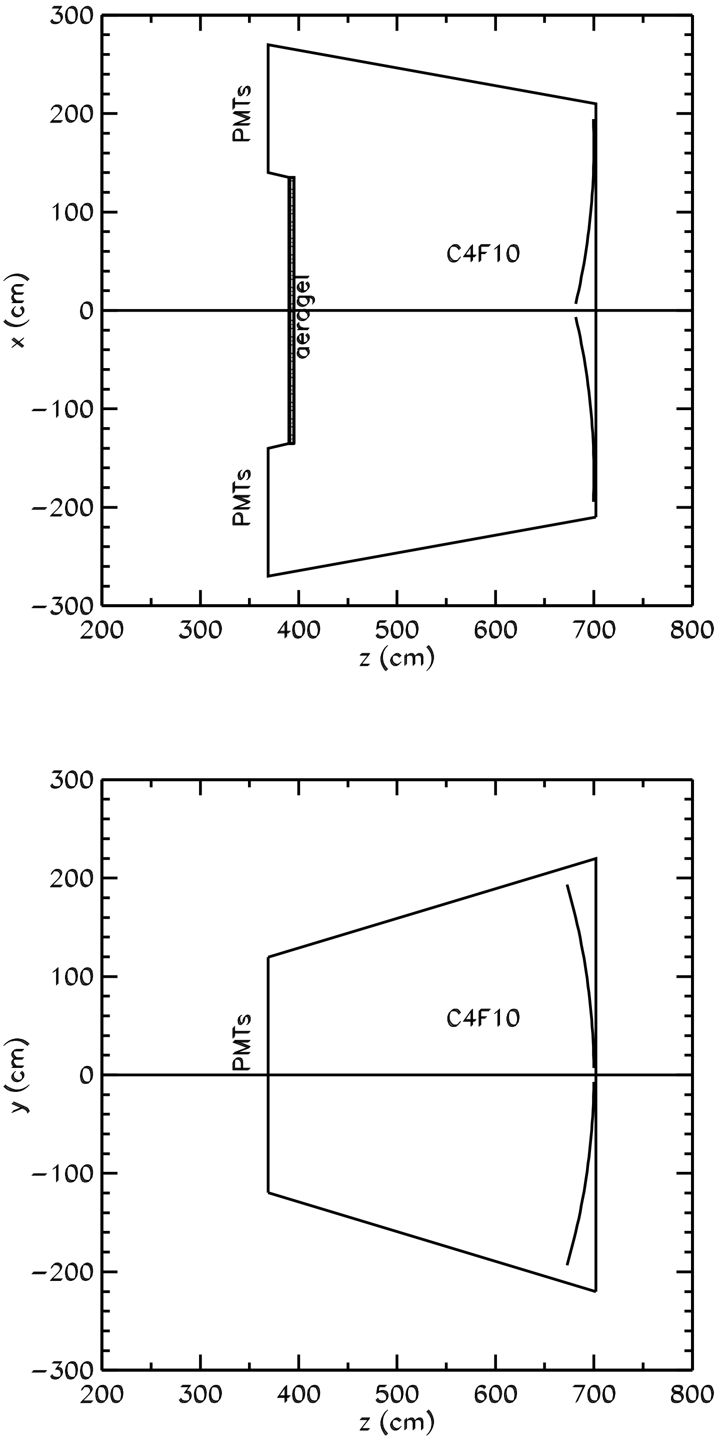

Figure 4.19: BTeV RICH geometry outline.

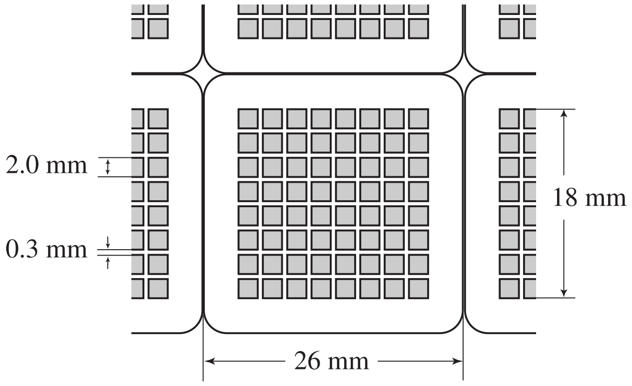

Figure 4.20: Closely packed array of Hamamatsu R5900-M64 tubes as seen from the front. The anode cells are shaded. The picture taken from Ref.[6].

4.2.5.4 Photo-detectors

The photo-detectors must be sensitive to visible wavelengths in order to detect Cherenkov rings from the aerogel. Because of the open geometry of the forward spectrometer and the absence of magnetic field around the RICH detector, arrays of photo-multipliers can be used. Detection of the Cherenkov spectrum in visible wavelengths allows the use of inexpensive window materials, standard photo-cathodes and a simple gas system. The photo-multiplier solution offers durability of the device. Large intrinsic gain and fast response provide for noise resistance and a straightforward read-out system. Hamamatsu has recently developed R5900 multi-anode photo-tubes (MAPMT) which are about 1 square inch in cross-section and are segmented into four, sixteen or sixty-four separate anodes. Thus, anode size can be selected to match other contributions to Cherenkov angle resolution. With the largest segmentation, the anode cell size is 2×2 mm. A closely packed array of R5900-M64 tubes is illustrated in Fig. 4.20. The multi-anode photo-tubes R5900-M16 were adopted for the HERA-B RICH detector [2]. The active photo-cathode area of R5900 tubes constitutes only about 50% of the total area of the tube (not including additional 0.3 mm wide dead spaces in between the anode cells).

To increase the geometrical efficiency, a light focusing system right in front of the PM array is needed. Some losses of light in the light collection system are unavoidable. HERA-B uses a two lens system to concentrate light on the active area of a MAPMT. The magnification of the HERA-B system is 0.5, thus the effective cell size is doubled relative to the true anode cell size and a single photo-tube is serving an area which is larger than its own dimensions (i.e. the tubes are not closely packed). UVT plexiglass lenses have a combined transmission efficiency of about 70% at larger wavelengths (including reflective losses) [2]. LHC-B has proposed a single lens system [6]. An array of convex-plano lenses is in direct optical contact with MAPMT windows (see Fig. 4.21). The MAPMT tubes are closely packed. To recover the inactive area of MAPMTs the magnification of the system is 0.7. Such a design provides almost full coverage of the photo-detection plane with the minimal effective anode cell size (2.8×2.8mm for R5900-M64 tube). There is just one refractive surface to pass, thus the reflective losses are minimized. LHC-B is also studying a light collection system based on light guides concentrating light into active parts of the anodes [8]. Such a system could even avoid small dead areas in between the anode cells which add up to 22% inefficiency for the R5900-M64 tube. Similar solutions will work for our RICH as well.

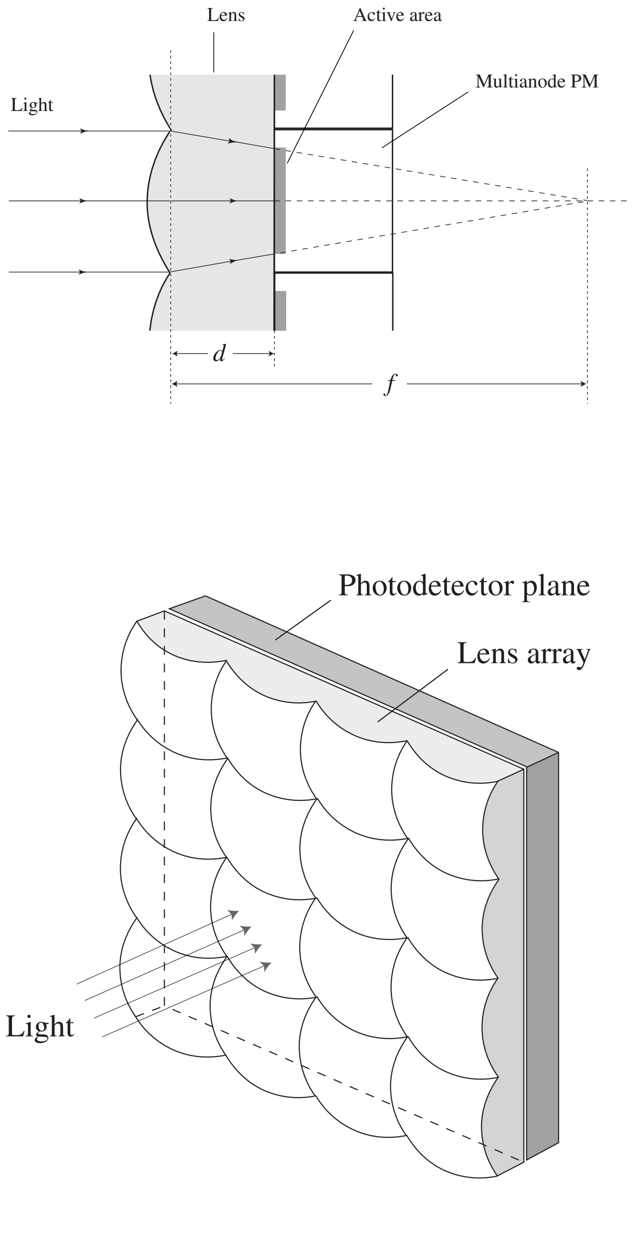

Figure 4.21: Two views of the lens system proposed by R. Forty for use with closely packed arrays of Hamamatsu R5900 MAPMTs. The pictures are taken from Ref.[6].

Hybrid Photo-Diodes offer an alternative photo-detection scheme. In an HPD, a photo-electron emitted by the photo-cathode is accelerated onto a silicon pixel detector by a very high voltage. Commercially available HPDs from DEP in the Netherlands have 61 closely packed hexagonal pixels, each with an area of 3.5 mm^2, enclosed in a single cylindrical tube (see Fig. 4.22). The active area of the tube is small, $\approx$30% of the total area. These HPDs were successfully used to detect Cherenkov photons in a beam-test setup by the LHC-B group [9]. To recover geometrical inefficiency, a light focusing system with a magnification of < 0.5 could be designed. An aggressive R&D program has been pursued at CERN to develop HPDs with a higher active area for LHC-B RICH detectors. This is mostly achieved by increasing the overall size of the vacuum tube to 80-127 mm in diameter, with a much larger number of pixels inside (1024-2048). To maximize the active area of the front face of the tube, photoelectrons are electrostatically focused onto a smaller diameter silicon pixel array inside, while being accelerated at the same time. Two different focusing schemes are under development. For such a large number of channels per tube it is impractical to have front-end electronic chips situated outside the tube. Thus, the read-out chips are being integrated into the vacuum tubes of HPDs. One of the new HPDs is being developed in collaboration with DEP. Even if suitable HPDs are available in the relevant time scale for BTeV, HPD technology has some drawbacks. Lower intrinsic gain ($5 \cdot 10^3$ vs 10^6 for MAPMT) requires more sophisticated read-out electronics. Also much higher voltages are required (20 kV vs 1 kV for MAPMTs). HPDs are more sensitive to fringe magnetic fields than MAPMTs. On the other hand, if the CERN R&D program succeeds, HPDs with a larger fraction of the active area may be available, perhaps eliminating the need for a light collection system in front of HPD arrays. The overall price for a full size detector is estimated, at present, to be comparable between the MAPMTs and HPDs.

We choose the MAPMT solution for the baseline design, however we intend to continue to evaluate HPD option as well.

4.2.5.5 Expected resolution for gaseous radiator

The emission point error magnified by the mirror tilt is about 0.4 mrad per photon, slightly dependent on the the exact charged track trajectory.

The chromatic error depends on the choice of photo-cathode, window and lens materials. Extending the transparency of the optical elements towards shorter wavelengths increases the chromatic error per photon. At the same time, the number of detected C_4F_{10} photons per track is also increased, making the Cherenkov angle resolution per track almost invariant. It should be noted that the increased wavelength sensitivity has no effect on photon yield and chromatic error for the aerogel radiator. Since materials with good UV transparency (e.g. quartz glass) are expensive, we assume standard borosilicate glass windows on MAPMTs. The dependence of quantum efficiency on photon energy used in the simulations is shown in Fig. 4.23. With this wavelength acceptance, the chromatic error per photon is expected to be 0.39 mrad, well matched to the emission point error.

The third significant contribution to the single photon resolution will come from a finite

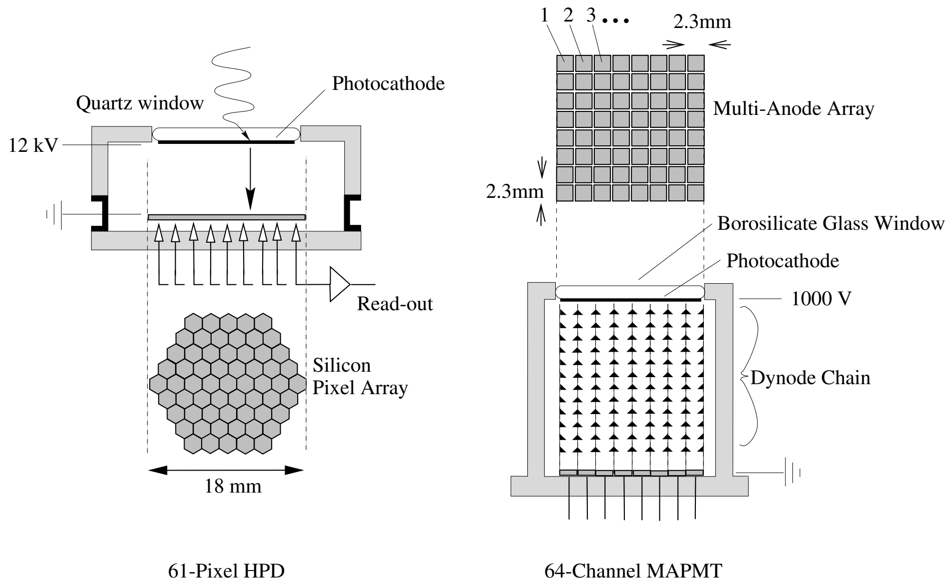

Figure 4.22: 61-Pixel HPD from DEP and R5900-M64 MAPMT from Hamamatsu. The pictures are taken from Ref.[7].

effective cell size of the photo-detector. For $d \times d$ cell size, this contribution is expected to be $\sigma_\theta = d/\sqrt{12} \times 2/R$. Closely packed R5900-M64 photo-tubes with the single lens light collection system described previously would result in a detector granularity error of 0.24 mrad, below the contributions from the emission point and chromatic errors. Covering the entire photo-detection area with the finest segmentation escalates the number of electronic channels and therefore, the cost of the detector. The best possible Cherenkov angle resolution is needed for high momentum tracks radiating photons in the the gaseous radiator. The higher momentum tracks tend to be closer to the beam pipe and illuminate a smaller region of the photo-detection plane than slower tracks. This region also has the highest occupancy of photons since the track multiplicity increases in the beam direction. For these two reasons, the inner region of the photo-detection plane must be populated with the finest segmentation. The outer region of the photo-detection plane is populated by C_4F_{10} photons from slower tracks. All aerogel photons tend to fall into the outer region too, because of the much larger value of the Cherenkov angle. This is fortunate, since low intensity aerogel rings would have been heavily contaminated by high intensity gaseous rings in the inner region. The Cherenkov angle resolution becomes less critical for slower tracks. Since occupancy is lower in the outer regions, it will be possible to populate these areas with coarser segmentation without a significant impact on the performance of the device. We intend to use R5900-M16 tubes here. In this region, the photo-detector segmentation error will be around 0.51 mrad and will dominate the C_4F_{10} Cherenkov angle resolution. To determine the boundaries of

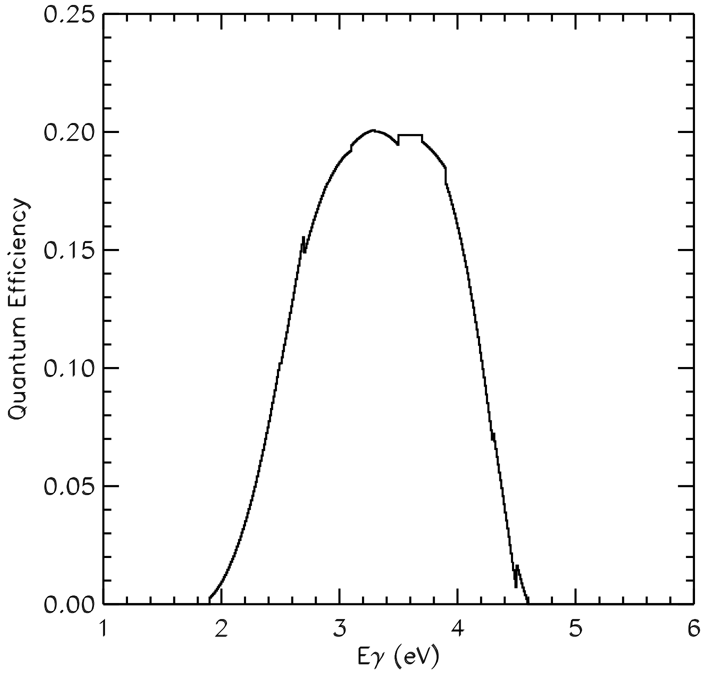

Figure 4.23: Quantum Efficiency of MAPMTs with borosilicate glass windows (as used in HERA-B RICH) used in our simulations.

the regions with fine and coarse segmentation of MAPMTs, we studied the occupancy of the photo-detection plane by various sources of Cherenkov photons. The distribution of photons produced in C_4F_{10} by the faster track in the reconstructed $B^0 \to \pi^+\pi^-$ events is shown in Fig. 4.24. This should be compared to the similar distribution of C_4F_{10} photons produced by all tracks from generic $b\bar{b}$ events shown in Fig. 4.25. The distribution of aerogel photons from generic $b\bar{b}$ events is also shown in Fig. 4.25. The selected regions of the fine and coarse MAPMT segmentation are indicated on these plots. In total, we intend to cover 3.1 m^2 of area in each of the two identical RICH detectors. The inner (1.2 m^2) part of this area will be finely segmented. Table 4.7 summarizes the number of tubes and electronic channels. The coarser segmentation in the outer photo-detection region has almost no effect on Cherenkov angle resolution for the faster track in the $B^0 \to \pi^+\pi^-$ events (2% effect). The resolution for the aerogel radiator is also not effected, since the chromatic error is large (see the next section). To match this error we could use R5900-M4 tubes in the outer region and further reduce number of electronics channels. However, such a scheme would deteriorate the C_4F_{10} high momentum resolution by 10%. Perhaps, another intermediate area with R5900-M16 tubes could fix the problem. Further optimization studies are needed.

Overall Cherenkov angle resolution per photon for the C_4F_{10} radiator is expected to be

PMT Tube type	Area	Number of tubes	Number of channels
R5900-M64	1.22 m^2	1800	115,200
R5900-M16	1.89 m^2	2800	44,800
Together	3.11 m^2	4600	160,000
Two RICH detectors	6.22 m^2	9200	320,000

Table 4.7: Number of Tubes and channels per detector arm and total in two arms.

0.61 mrad. Per track resolution depends on the observed photo-electron yield.

In addition to quantum efficiency losses, photo-electron yield is reduced by imperfect mirror reflectivity, absorption in light collection and PMT window materials and reflective losses on refractive boundaries. The MAPMT tubes also have a small inactive area in between anode cells. This effect has been recently studied for R5900-M64 tubes by the Oxford group [10]. Their measurement (23% light loss) comes close to the naive expectation from the geometrical dimensions of the anode cells and the dead area in between. We simulate this effect explicitly in a geometrical way. Loss of light yield due to finite cell size (photon overlaps) is about 5.5% for saturated rings, and is also modeled explicitly. For mirror reflectivity we assume 87%. In the HERA-B light collection system, there are five refractive boundaries resulting in 15% light loss due to reflections on these surfaces [2]. There is only one refractive boundary in the light focusing scheme described above, thus we assume only 4% loss. Finally, we assume 20% loss for absorption in the light collection system compared to 15% estimated for the HERA-B lens system. After all these corrections the average photo-electron yield from C_4F_{10} for $\beta = 1$ particles is expected to be close to 50. LHC-B expects to achieve a similar photo-electron yield with a 3 times shorter C_4F_{10} radiator. This is mostly (factor of 2.3) due the quantum efficiency assumed by LHC-B, which extends towards much shorter wavelengths. The rest can be accounted for by a more optimistic assumption about light collection efficiency. Even though the extended wavelength coverage increases photo-electron statistics, chromatic error is also increased producing almost no gain in Cherenkov angle resolution per track. To maintain wide wavelength coverage expensive window and light collection materials would have to be used. Therefore, we prefer to work in a narrower range of wavelengths. Our estimated photo-electron yield is larger than projected for the HERA-B RICH (32-35 photo-electrons)[2]. This is partially due to a different light collection scheme assumed here, and the lack of a second mirror in our design.

Our simulations predict the average Cherenkov angle resolution per track from the C_4F_{10} radiator to be 0.0935 mrad. The resulting K/π separation at higher momenta is shown in Fig. 4.26. The projected performance satisfies our physics goals well. Various contributions to Cherenkov angle resolution are summarized in Table 4.8.

Table 4.8: Expected performance of BTeV RICH system.

	C_4F_{10}	Aerogel $n = 1.03$
emission point error	0.4 mrad	0.1 mrad
chromatic error	0.4 mrad	1.9 mrad
segmentation	0.2 mrad	0.5 mrad
total error per photon	0.6 mrad	2.0 mrad
number of photons	50	9
total error per track	0.094 mrad	0.7 mrad

4.2.5.6 Expected resolution for aerogel radiator

The chromatic error for aerogel photons is expected to be about 1.9 mrad. This is likely to be an overestimate since we did not simulate attenuation of shorter wavelengths in the radiator itself. The effect of the lucite filter between the aerogel and gas radiators was simulated as a sharp cut-off at 300 nm.

HERMES reports [3] additional 0.7 mrad error, mostly due to aerogel density variation. The emission point error is expected to be very small (0.09 mrad) because the radiator in only 5cm thick. The detector granularity error is below 0.51 mrad. Putting all these factors together we predict the Cherenkov resolution per photon to be around 2 mrad.

We assume 9 detected photo-electrons per track according to the recent reports from HERMES. This photon yield cannot be increased by using a thicker radiator because of light scattering and absorption in aerogel itself. Further improvements in aerogel transparency would increase the number of photons per Cherenkov ring.

The expected Cherenkov resolution per track is about 0.7 mrad. The resulting K/p separation at lower momenta is shown in Fig. 4.27. The required K/p separation up to the proton Cherenkov radiation threshold in C_4F_{10} should be easily achieved. Various contributions to Cherenkov angle resolution are again summarized in Table 4.8.

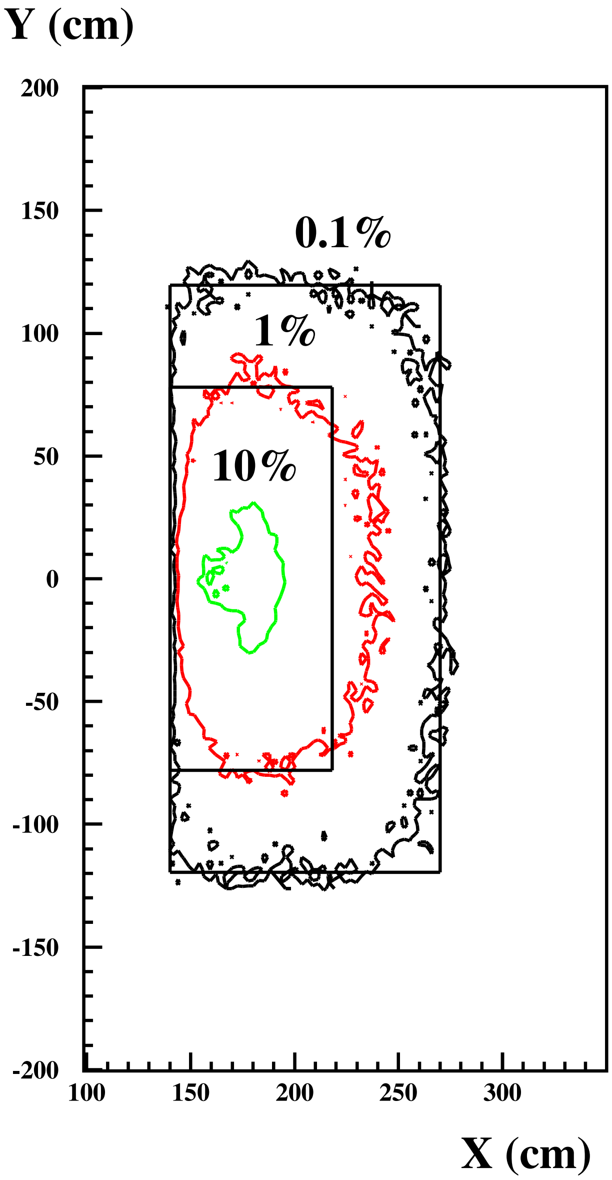

Figure 4.24: Contours of the number of Cherenkov photons per one MAPMT (2.6×2.6 cm^2) per event produced in C_4F_{10} by the faster track in reconstructed $B^0 \to \pi^+\pi^-$ decays. Rectangular boxes illustrate areas to be covered with MAPMTs. The inner box corresponds to the region of finer segmentation.

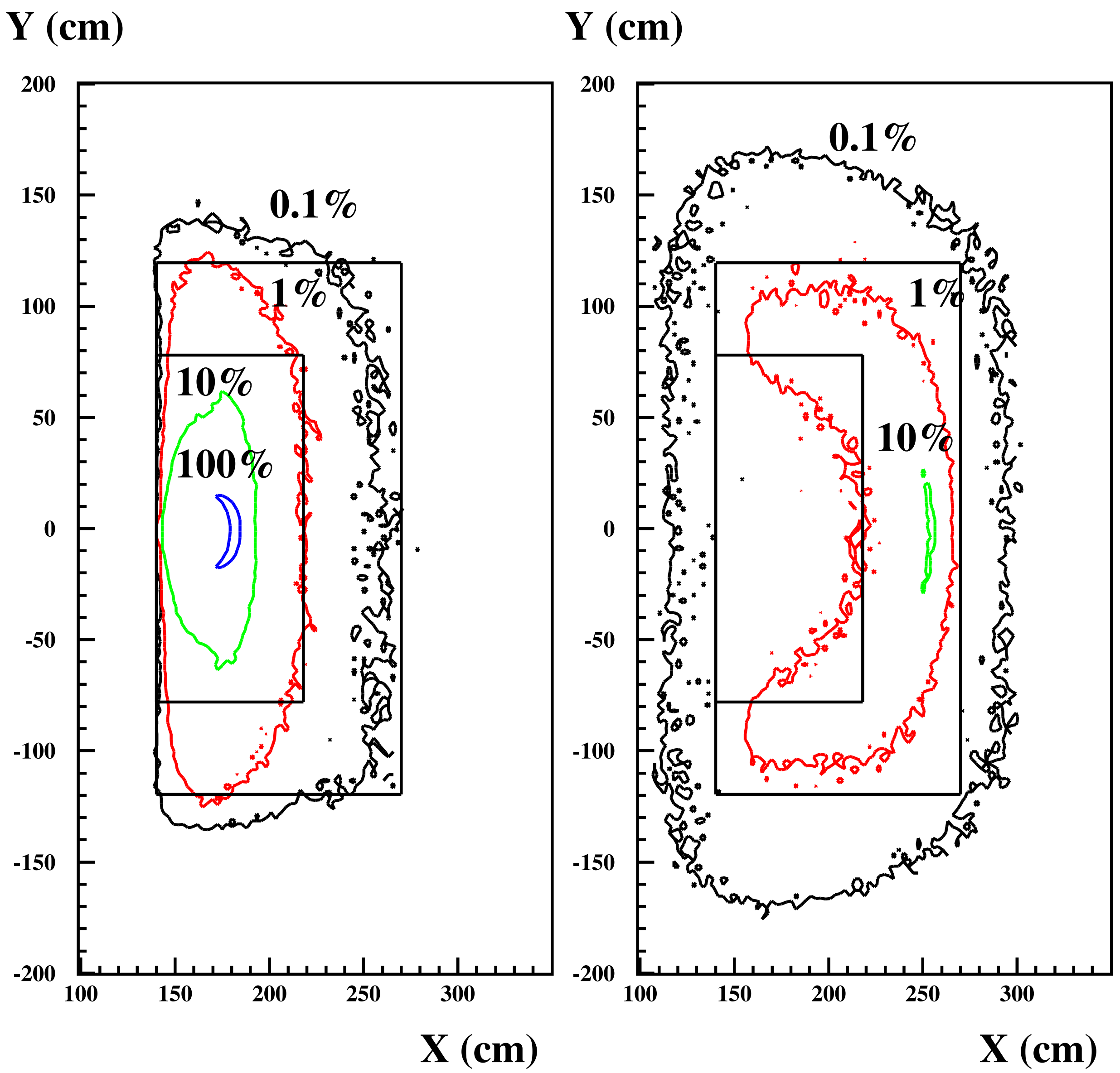

Figure 4.25: Contours of number of Cherenkov photons per one MAPMT (2.6×2.6 cm^2) per event produced by all tracks in generic $b\bar{b}$ event originating from C_4F_{10} (left) and aerogel (right) radiators. Rectangular boxes illustrate areas to be covered with MAPMTs. The inner box corresponds to the region of finer segmentation.

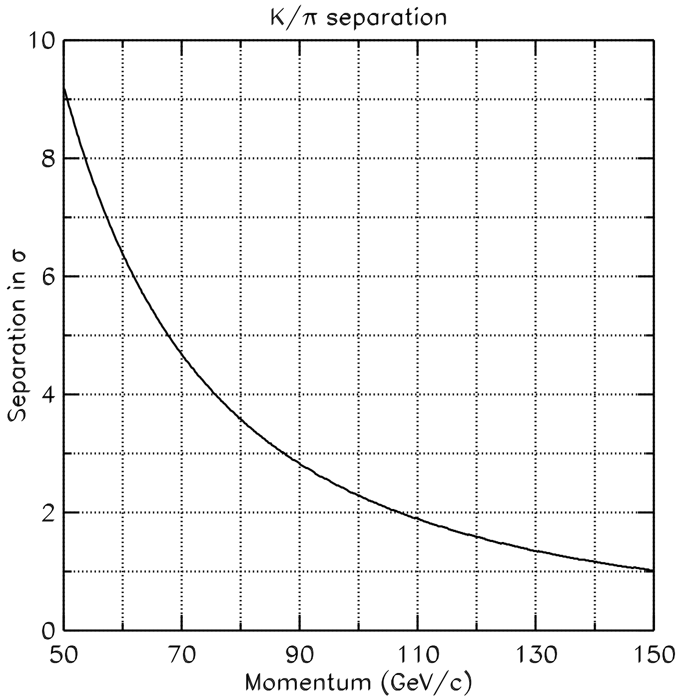

Figure 4.26: Expected K/π separation from C_4F_{10} radiator.

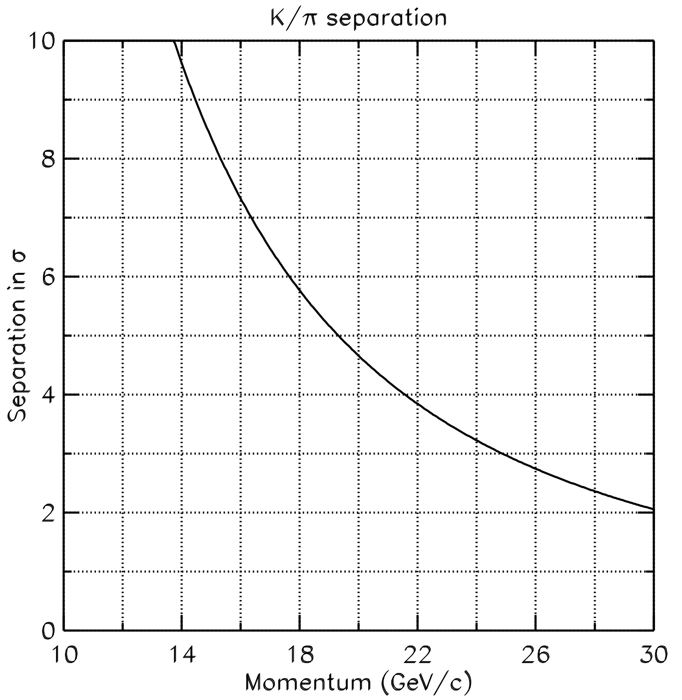

Figure 4.27: Expected K/p separation from aerogel radiator.

Bibliography

[1] W. Adam et al., Nucl. Inst. & Meth. **A343**, 60 (1994).

[2] J.L. Rosen, Proceedings of The Fifth International Workshop on $B-$Physics at Hadron Machines, Los Angeles, USA, Oct. 13-17, 1997, published in Nucl. Inst. and Meth. A408 (1998) 191; S. Kopar, Proceedings of the The 3rd International Workshop on Ring Imaging Cherenkov Detectors Weizmann Institute of Science Ein-Gedi, Dead-Sea, Israel, Nov. 15-20, 1998.

[3] P. Carter, Proceedings of the The 3rd International Workshop on Ring Imaging Cherenkov Detectors Weizmann Institute of Science Ein-Gedi, Dead-Sea, Israel, Nov. 15-20, 1998. "Proposal for Dual Radiator RICH for HERMES", E. Cisbani et al., Hermes Internal Note 97-005.

[4] LHC-B, Technical Proposal, CERN LHCC 98-4, LHCC/P4, 1998.

[5] R. Forty, CERN-PPE/96-176, Sept. 1996 published in Proc. of the 4^{th} Int. Workshop on $B-$physics at Hadron Machines, Rome, Italy, June 1996, F. Ferroni, P. Schlein (Eds.), North-Holland, 1996.

[6] R. Forty, "Use of lenses to increase the RICH photo-detector coverage", LHCb Internal Note LHCB/98-038.

[7] A. Duane et al., LHCb Internal Note LHCB/98-039.

[8] V. Grecco, A. Petrolini, "Study of a possible light collector system for multi-anode photo-multiplier tubes", LHCb Internal Note LHCB/99-005.

[9] S. Easo, Proceedings of the The 3rd International Workshop on Ring Imaging Cherenkov Detectors Weizmann Institute of Science Ein-Gedi, Dead-Sea, Israel, Nov. 15-20, 1998.

[10] N. Smale et al., "Evaluation of the multi-anode photo-multipliers for the LHCb RICH detectors", LHCb Internal Note LHCB/98-066.

4.2.6 Electromagnetic Calorimetry

4.2.6.1 Introduction

A thorough investigation of B decays requires the ability to study decay modes containing single photons, π^o's, and η's. Some of the important decay modes mentioned in chapter 1 are:

- $B^o \to (\rho\pi)^o \to \pi^+\pi^-\pi^o$;
- $B^o \to K^{*o}\gamma$ and $\rho^o\gamma$;
- $B_s^o \to \psi\pi^o,\ \psi\eta,$ and $\psi\eta^{'}$;
- $B^o \to K^{*o}\pi^o$; and
- $B^\pm \to K^\pm\pi^o$ and $\pi^\pm\pi^o$.

We have begun an intensive study of the problems associated with reconstructing electromagnetic showers in the environment of a hadron collider and using them to obtain signals for B mesons containing photons in the final state. While this study is still in progress, we are sufficiently encouraged by our initial results to develop a baseline design for an electromagnetic calorimeter which is capable of reconstructing photons. The electromagnetic calorimeter will also be used to identify electrons which can be used to tag the flavor of the associated B for CP studies or to isolate high mass electron-positron pairs that form exclusive final states. Examples are $B \to D^{(*)}e\nu$ (for electron tagging) and $B \to J/\psi K_\mathrm{s}$, $J/\psi \to e^+e^-$, $K_\mathrm{s} \to \pi^+\pi^-$.

Below in chapter 11, we discuss the challenges of isolating the small signals of the most interesting decay modes from the large backgrounds that are encountered in hadronic interactions. Here, we present the key requirements on energy and position resolution and on radiation hardness that the calorimeter must satisfy. We then present the BTeV baseline electromagnetic calorimeter design. In chapter 11, we show simulations of key signals and in chapter 14 we present a preliminary cost estimate for the proposed baseline device.

4.2.6.2 Key Requirements and Issues

To determine the appropriate size, segmentation, and technology for the calorimeter requires an understanding of the kinematic properties of the photons in signals, of potential sources of backgrounds, and of the radiation environment.

The area available to the calorimeter is located about 7.0 meters from the nominal interaction point and extends in Z for 1 meter. The distance from the beam to the floor is 2.5m. The transverse dimension which matches the acceptance of the spectrometer is a 4 x 4 meter box centered on the Tevatron beam line.

We have begun very detailed Monte Carlo studies of the following two benchmark processes to understand the signals we hope to measure:

- $B^o \to K^{*o}\gamma$ and
- $B^o \to \rho^+\pi^-, \rho^-\pi^+,$ and $\rho^o\pi^o$.

The results of the full simulation are presented in chapter 11. Here, we present only the 'generator level' study for $K^*\gamma$ and for $B^o \to \rho^+\pi^-$. In the first study, we simply require all tracks of the final state of interest to be within the angular acceptance of the BTeV spectrometer and to satisfy a minimum energy requirement. We chose these two modes because the photon in the $K^*\gamma$ decay has rather high momentum and P_t, while those from the π^o decay of the ρ^+ are much softer. The results of these studies are shown in Fig. 4.28 and Fig. 4.29. Based on these studies, the energy range of interest is extends from 1 GeV to 60 GeV and the angular range of interest extends out to 200-300 milliradians.

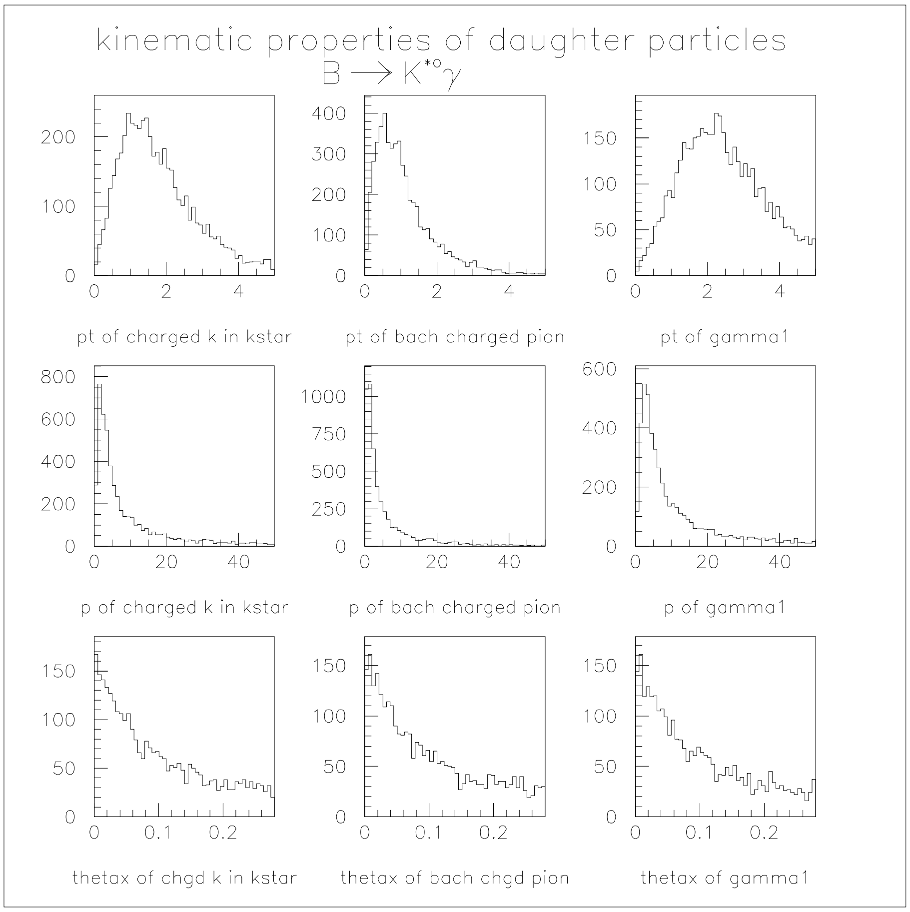

Figure 4.28: Kinematic properties of $B \to K^*\gamma$ where all generated tracks satisfy rudimentary acceptance requirements

To understand the requirements on energy and angular resolution, we have done a more sophisticated simulation. In this simulation, we carried out a full Monte Carlo generation and offline tracking of the charged tracks. For the photons, we smeared the momentum vectors

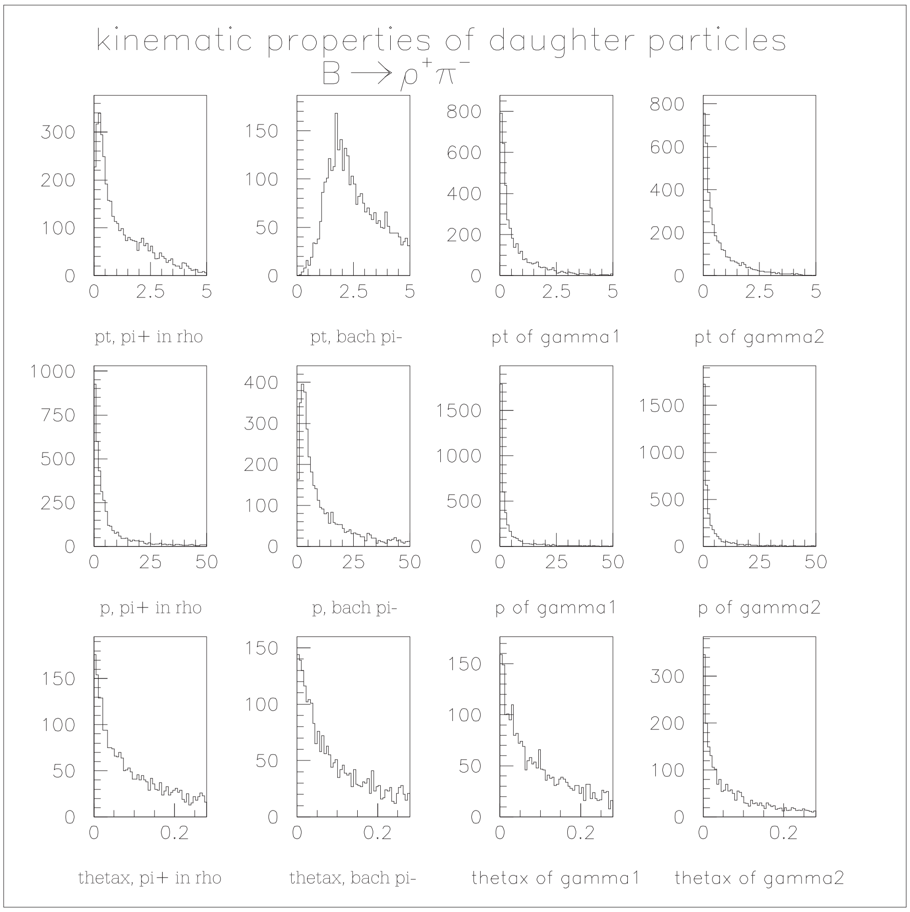

Figure 4.29: Kinematic properties of $B^o \rightarrow \rho^+\pi^-$where all generated tracks satisfy rudimentary acceptance requirements

of the generated photons in energy and angle and used the smeared momentum vectors in mass calculations. The energy is smeared according to

$$\frac{\sigma_E}{E} = \sqrt{\frac{a^2}{E} + b^2} = \frac{a}{\sqrt{E}} \oplus b, \tag{4.3}$$

with E in units of GeV. We refer to the parameters a and b as the stochastic term and the constant term, respectively. The angles were smeared by projecting the generated γ to the surface of the calorimeter, smearing the position there using a Gaussian of width $\Delta X/\sqrt{12}$ and $\Delta Y/\sqrt{12}$, where ΔX and ΔY are the transverse dimensions of the calorimeter elements. The angles were recalculated (using the primary vertex for the upstream point). Finally, a smeared γ momentum vector and its correctly propagated covariance matrix were calculated. These are used together with the charged tracks found in the offline analysis to reconstruct the B mass. The parameters a, b, ΔX, and ΔY can be varied and their effect on the mass resolution and other quantities can be obtained. Some results from these studies are given below in Table 4.9. The results agree well with the results from the full MCFAST simulation and shower reconstruction shown later.

4.2.6.3 Backgrounds

There are two major issues concerning backgrounds which influence the requirements on the calorimeter. The first has to do with problems in the reconstruction of objects – γ's, π^o's, electrons, η's, etc. – which can result in poor efficiency, the reconstruction of 'false' objects, and the reconstruction of objects with seriously degraded resolution. The second has to do with combinatoric backgrounds – that is, not knowing which of the many neutral objects appearing in a typical event to associate with the decaying B. We have learned that the backgrounds due to problems in object reconstruction place the most demanding requirements on the detector, except for the energy resolution which determines the overall mass resolution of the final state. Good mass resolution is a final defense against combinatoric backgrounds. In this section, we discuss the requirements that help reduce the object reconstruction backgrounds. Methods for defeating combinatoric backgrounds are discussed in chapter 11 below.

The dominant processes which mimic a single photon are:

- High momentum π^o's whose two photons are emitted within a very small angle. Because of the finite size of the calorimeter elements and of the electromagnetic shower, these can appear to merge or 'coalesce' into a single shower. Since there is an energy dependent minimum opening angle between the photons in π^o decay, this problem affects mainly the highest energy photons of interest to BTeV. A high degree of segmentation can reduce this background and an analysis which uses transverse shower shape variables can be effective at detecting coalesced photons up to quite high energies. Below we show that coalesced photons can be identified up to over 90 GeV with the proposed baseline calorimeter.

- π^o decays where the less energetic of the two photons is below the sensitivity of the calorimeter or falls outside the calorimeter's geometric acceptance. A π^o can decay so one photon takes most of the energy while the other photon has very little. If the ability exists to detect the low energy photon, it can be paired with the higher energy single photon candidates to see if they form a π^o and if they do, those high energy photons can be rejected as single photon candidates. However, since the BTeV calorimeter is far from hermetic, this approach is not very efficient. Instead, one has to understand which states containing π^o decays are potential sources of fake single photon signals and demonstrate that they have not polluted the single photon signal. For example, the decay $B^o \to K^{*o}\pi^o$ can mimic $B^o \to K^{*o}\gamma$ if the π^o decays very asymmetrically.

The dominant source of background to π^o identification is combinatoric background. All pairs of photon candidates (some of which will be false) must be considered in reconstructing π^o's. Random pairings make a rather smooth background in invariant mass. Since the mean number of photons recorded in the calorimeter in a typical B event is 30, the total number of combinations is very large. Many of the photons are unpaired – that is they come from a π^o, η^o or other parent but one of the daughter photons is outside the calorimeter's acceptance or below its energy sensitivity. Coalesced π^o's also mimic individual photons and participate in incorrect pairings. Shower overlaps both with other photons and hadronic showers in the calorimeter can distort the energy and angles of the photons and push the π^o masses to an incorrect value. Converted photons produce e^+e^- pairs which can bremsstrahlung, producing other photons that create background. The signal to background ratio of the π^o signal depends on the energy resolution since the narrower the π^o mass peak, the smaller is the integrated background under it.

Electrons will be identified by matching their energy with the momentum measured for the track by the spectrometer ($\frac{E}{p}$) and by looking at their transverse profiles. The dominant background which results in the false identification of objects as electrons is expected to be photon conversions due to interactions in the beam pipe, in the silicon near the primary vertex, or in the material of the RICH or forward tracker elements. Other backgrounds will be misidentified charged pions which charge exchange early in the calorimeter, and other rare processes which can mimic the behavior of an electron.

The ability to reject backgrounds will depend on the choice of the calorimeter technology, the segmentation, and to some extent the performance of the other detector elements. These processes are being evaluated with Monte Carlo tools (such as GEANT and MCFAST) and perhaps eventually with test beam studies.

We have identified combinatoric background as a serious problem. A final defense against the combinatoric background is mass resolution. The calorimeter is the only means of measuring the energy and angles of neutral objects in the event. The energy resolution of the calorimeter is a more significant source of mass smearing than its angular resolution. For the range of calorimeter technologies satisfying other BTeV requirements, the energy measurement of the photons will dominate the total mass resolution of the state. Table 4.9 shows the mass resolution for $B^o \rightarrow K^{*o}\gamma$, using an energy resolution parameterized as above with stochastic terms of 3.0%, 2.5%, 2.0%, and 1.5% and constant terms of 1.0%, 0.75%, and 0.55%, and 0.25%. Both the constant and stochastic terms are important contributors to the resolution because of the large energy range of the photons.

Table 4.9: Mass Resolution for Different Calorimeter Energy Resolutions (statistical accuracy is 2-3 MeV/c^2)

State	a %	b %	Mass Resolution MeV/c^2
$B^o \to K^{*o}\gamma$	3.0	1.0	54
	2.5	1.0	48
	2.0	1.0	49
	1.5	1.0	49
	3.0	0.75	46
	2.5	0.75	50
	2.0	0.75	42
	1.5	0.75	39
	3.0	0.55	45
	2.5	0.55	41
	2.0	0.55	44
	1.5	0.55	40
	3.0	0.25	41
	2.5	0.25	45
	2.0	0.25	40
	1.5	0.25	36

4.2.6.4 Radiation Hardness Requirements

A full calculation of the radiation environment takes into account radiation deposited in the calorimeter from the direct products of collisions, from the interactions of those products with the material of the spectrometer, from beam halo, and from backscatter and residual radiation from other detectors. We are in the process of carrying out such a calculation, but it is not yet complete. Here, to get an idea of the radiation environment the detector must tolerate, we show, Fig. 4.30 the energy dose in the calorimeter from photons, electrons, interacting hadrons, and non-interacting charged particles per (minimum bias) interaction. We set the radiation requirement based on tripling the deposition from these events to account for sources not included in this calculation. The calorimeter begins at ± 9.88 cm in both X and Y. The annual radiation dose is 60 KGrays at a radius of about 14 cm (20 mr). The dose falls off like a power of the radius to the 2.3 power from 20 cm on out. The detector needs to be radiation hard towards the middle and radiation tolerant on the outside. At 20 mr, the detectors nearest the beam will receive doses that are a quarter of those expected at the LHC (at greater radius but much higher luminosity and energy). We plan to use a solid state chip (the QIE) to digitize the pulse in or near the photomultiplier tube base. The radiation levels at the downstream end of the detector are therefore also of concern.

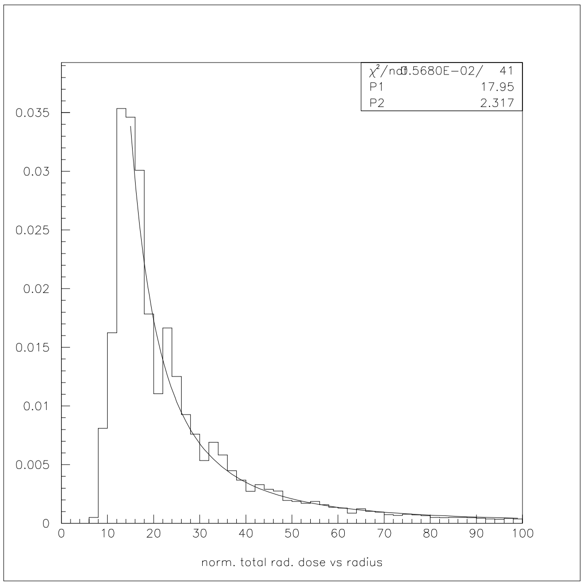

Figure 4.30: Total energy deposition in GeV per cm^2 per interaction (minimum bias) vs radius (cm) due to photons, electrons, interacting hadrons, and non-interacting (minimum ionizing) particles. The curve is the result of a fit to a power law, $A \times R^n$. The best fit gives $n = -2.3$. A rough conversion gives 20 KGrays/year for each 0.01 GeV per cm^2 per interaction.

4.2.6.5 Time resolution

The spacing of beam crossings at the Tevatron will be 132 ns. As long as the occupancy is low and there is some way of tagging which beam crossing each hit goes with, it is not necessary to have a signal which is so fast that it can be collected between crossings. However, it is certainly a convenience if this can be accomplished and may also reduce machine backgrounds as well.

4.2.6.6 Summary of Requirements

The above considerations lead to a range of requirements on various characteristics which are shown in Table 4.10. These requirements are not uniquely determined by our studies. They also reflect our current understanding of available technologies and their limitations. So, they have certain compromises already built in to them.

4.2.6.7 Baseline Technology

Several technologies were considered (from the point of view of performance, cost, and availability), including:

- A sampling calorimeter with lead and either scintillator or liquid argon

Table 4.10: Requirements of Baseline Electromagnetic Calorimeter

Property	Value
Maximum length	1 meter
Angular Resolution	1 mr at 700 cm
Energy resolution:	
Stochastic Term	1-3%
Constant Term	0.55-0.75%
Minimum angle	10-20 mr at 700 cm
Maximum angle	200-300 mr
Length	25 radiation lengths
Pulse pair resolution	must be able to associate pulse height to individual beam crossings with low pile up

- A total ionizing calorimeter based on either CsI or liquid krypton
- A calorimeter based on $PbWO_4$ crystals.

Of these, lead and scintillator was rejected because of poor resolution. Fermilab is reluctant to deal with the numerous safety issues related to operating liquid argon or liquid krypton in the C0 enclosure. These devices also have long charge collection times which can, however, be overcome by careful pulse shaping. Liquid krypton, in particular, looked like an attractive possibility. Liquid detectors are radiation hard. However, the constant term in the energy resolution may be considerably larger due to the relatively large amount of material before the active sampling material. CsI (undoped) was attractive from many points of view. However, it is not radiation hard enough to be used close to the beam. Furthermore, it is not quite fast enough to completely produce all its charge in under one crossing but it this problem is easily overcome with electronics that samples two or three crossings. Lead glass has been rejected because it is not likely to survive the yearly radiation dose.

After study, we have selected for our baseline a calorimeter made of $PbWO_4$ crystals. The BTeV $PbWO_4$ choice for an Electromagnetic Calorimeter (EMC) is largely based on the work of CMS. Our choice is based on several considerations, listed roughly in order of priority:

- It satisfies our requirements on energy and spatial resolution. Blocks of size roughly 2.5 cm can be made. CMS expects to achieve a stochastic term of 2.7% and a constant term of 0.55% using Avalanche PhotoDiodes (APDs) for readout. We plan to use photomultiplier tubes (PMTs) and expect to do better.
- This material is very resistant to radiation damage, especially when doped with either Nb or La. CMS requires the crystals to survive a dose of 50 kGy. This should be sufficient for BTeV.

- They are fast – they deliver 99% of their light output within 100 ns.

The properties of $PbWO_4$ which are important for the calorimeter are given in Table 4.11.

We describe some properties of the CMS calorimeter for purposes of comparison with the device we are proposing. CMS has chosen $PbWO_4$ for both barrel and endcaps. The crystals are tapered to point at the interaction region. The sizes differ, the barrel crystals are 230 mm long, while the endcap crystals, which follow a 5 radiation length preradiator, are 220 mm long. The endcaps are 24.7 mm square in the front, while the barrel counters are smaller at 21.5 mm square. BTeV will use untapered blocks of very similar dimensions. Many details about the $PbWO_4$ calorimeter can be found in the CMS writeup [1].

CMS will use Avalanche Photodiodes (APD) to read out the barrel and Vacuum Phototriodes to read out the endcap. These devices are necessary because of the high magnetic field in which the crystals are positioned. In BTeV we are far from any magnetic fields, so we can use photomultiplier tubes. This provides less noise, better resolution as will be described below, in a well understood and tested technology. In fact, BTeV could use the same tubes that KTeV used for their inner blocks, the Hamamatsu R5364, provided that a radiation hard glass such as C96-1 is used.

As part of its acceptance criteria, CMS requires that all of their crystals emit more than 10 photoelectrons per MeV into a XP2262B photomultiplier tube covering the back face of the crystal. Using a smaller phototube, we expect to collect in excess of 7 photoelectrons per MeV. CMS actually collects ≈4 photoelectrons per MeV into two 25 mm^2 APD's on each crystal.

Table 4.11: Properties of $PbWO_4$

Property	Value
Density (gm/cm^3)	8.28
Radiation Length (cm)	0.89
Interaction Length (cm)	22.4
Light Decay Time (ns):	5(39%) 15(60%) 100(1%)
Refractive Index	2.30
Maximum of emission (nm)	440
Temperature Coefficient (%/^{o}C)	-2
Light output/NaI(Tl) (%)	1.3
Light output (pe/MeV into a 2" PMT)	10

Despite all the work that has been done by CMS, there are significant open issues and risks in this approach. The main problem is growing crystals with sufficient quality and reproducibilty (yield), to lead to acceptable costs. There are only four producers working with CMS which currently have the ability to grow these crystals, and they will be kept busy for some time producing the crystals for CMS. These companies are in the Czech Republic, Russia and two in China. We will attempt to look for new sources, however.

It may be possible to use another less radiation hard crystal at the periphery of the detector and we are evaluating such alternatives. However, in this document, we describe a system made totally from $PbWO_4$ crystals.

4.2.6.8 GEANT Studies

The EMC geometry was defined as a rectangular array of crystals 24.7x24.7 mm^2. The length of the crystals was varied. A full simulation of the material properties was done with photons normally incident on the array, but smeared over the front face of the crystals.

i. Crystal length

We first explored the desired crystal lengths. In Figs. 4.31 and 4.32, we show the total energy deposited in the crystal for 2.5 GeV/c and 80 GeV/c incident photons, representing a low energy and an energy near the upper range of interest.

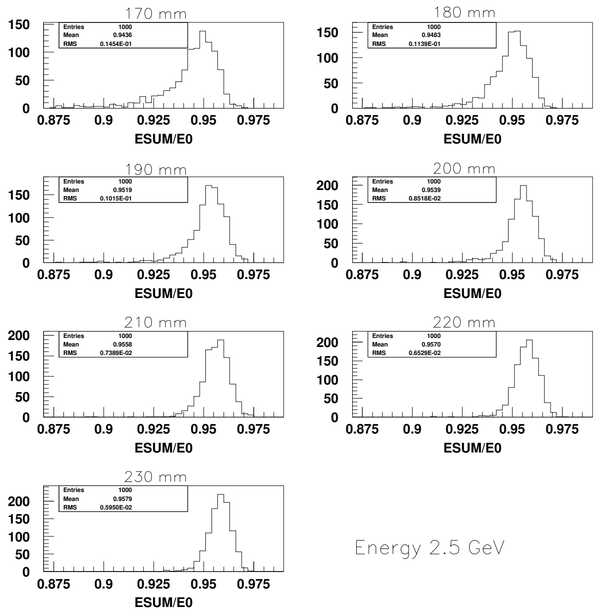

Figure 4.31: Energy deposited for 2.5 GeV/c photons normally incident on $PbWO_4$ crystals of the labeled lengths.

It appears that 220 or 230 mm lengths are required. In order to make this study more quantitative, we clustered the energy in a 5x5 array of crystals centered on the crystal with the largest energy deposit. Then we fit the distributions with a function that reasonably describes the central part of the distribution as a Gaussian with an asymmetric low energy tail. This function has been called the "Crystal Ball lineshape," and was named after a former experiment based on NaI crystals [2]. The function form is

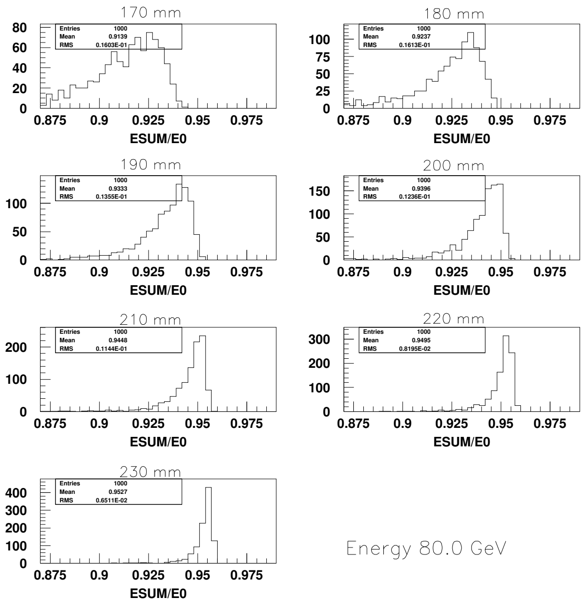

Figure 4.32: Energy deposited for 80 GeV/c photons normally incident on $PbWO_4$ crystals of the labeled lengths.

$$f(E|E^*, \sigma_{E^*}, \alpha, n) = \left(\begin{array}{ll} A \cdot \exp\left[-\frac{1}{2} \left(\frac{E^* - E}{\sigma_{E^*}} \right)^2 \right] & \text{for } E > E^* - \alpha \cdot \sigma_{E^*} \\ A \cdot \frac{\left(\frac{n}{\alpha}\right)^n e^{-\frac{1}{2}\alpha^2}}{\left(\frac{E^* - E}{\sigma_{E^*}} + \frac{n}{\alpha} - \alpha \right)^n} & \text{for } E < E^* - \alpha \cdot \sigma_{E^*} \\ \text{here } A^{-1} \equiv \sigma_{E^*} \cdot \left[\frac{n}{\alpha} \cdot \frac{1}{n-1} e^{-\frac{1}{2}\alpha^2} + \sqrt{\frac{\pi}{2}} \left(1 + \text{erf}\left(\frac{\alpha}{\sqrt{2}} \right) \right) \right] & \end{array} \right. \tag{4.4}$$

Here E is the measured energy, E^* is the "true" (or most likely) energy and σ_{E^*} is the energy resolution. To use this formula, the parameter n is fixed to value of about 5.

GEANT events for different energy photons and lengths were fit with this function for different energies and lengths varying from 210 to 230 mm. An example of such a fit is shown in Fig. 4.33.

The result of this study is summarized on Fig. 4.34, where the σ from each of the the fits is plotted. We see that the energy resolution determined by the crystal length and transverse size is hardly affected by using crystals of 220 mm, but there is a degradation going to 210 mm. This study uses energy deposited in the 5x5 array of blocks without the smearing due to photon statistics, so the resolutions are unreasonably good.

The energy resolution determined without photon statistics or electronic noise for 220

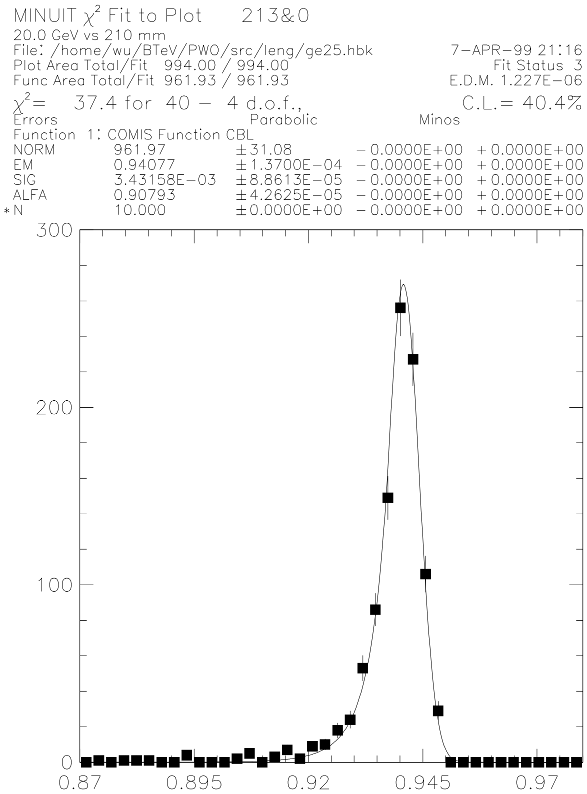

Figure 4.33: Fit of clustered energy deposited for 20 GeV photons normally incident on $PbWO_4$ crystals of 210 mm in length using the Crystal Ball lineshape. The x-axis is normalized to one at 20 GeV.

mm long crystals is shown on Fig. 4.35.

$$\sigma_E = \sqrt{\frac{a^2}{E} + b^2} \equiv \frac{a}{\sqrt{E}} \oplus b, \tag{4.5}$$

with $a = 1.08\%$ and $b = 0.2\%$, and E in units of GeV.

We can determine the component purely due to transverse leakage by fitting the distributions for total energy deposit and subtracting in quadrature the σ's from these fits and those with the 5x5 clustering. The transverse leakage component is shown in Fig. 4.36. We see the effect of transverse leakage can be characterized as

$$\sigma_E^{trans} = \frac{0.7\%}{\sqrt{E}}. \tag{4.6}$$

The transverse leakage component is sufficiently small that it is not necessary to attempt to add in more blocks to the energy sum

ii. Expected Energy Resolution

The final resolution in energy that we can expect from a $PbWO_4$ system will depend on several factors. One of these, is the transverse and longitudinal leakage. Another is

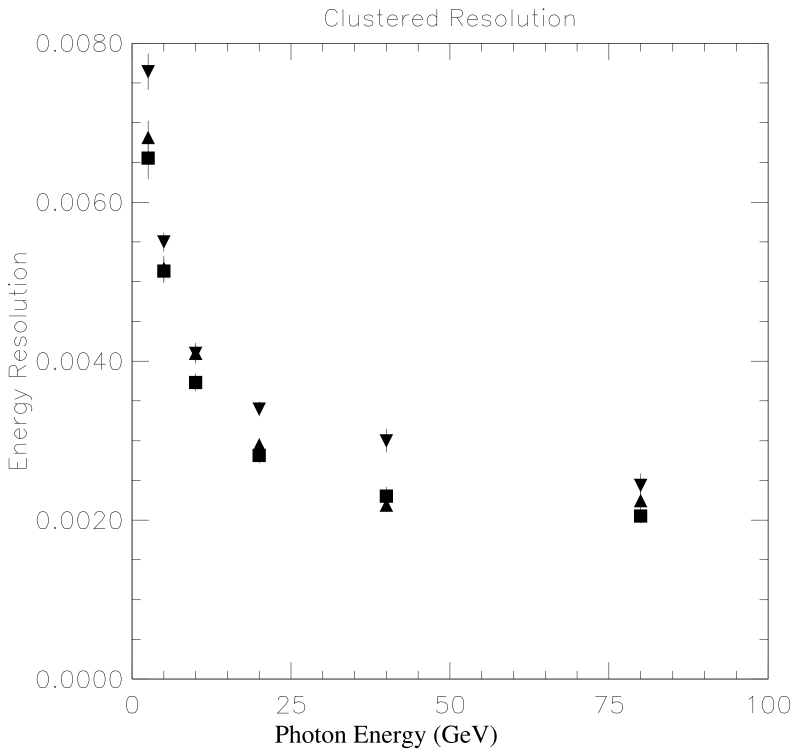

Figure 4.34: Energy resolutions as a function of incident photon energy for different crystal lengths using 5x5 clustering. The squares are for 230 mm, the triangles for 220 mm and the inverted triangles for 210 mm.

photoelectron statistics. These contribute to the so called "stochastic" term which has a $1/\sqrt{E}$ dependence. We will evaluate this term below. Other effects that could contribute include electronics noise, negligibly small for phototubes, variations in light output along the crystal length, errors in the relative calibration between crystals, and possible other yet to be identified sources. These latter effects contribute to the "constant" term.

We can use the energy resolution expected by CMS to guide our expectations. They base their study on 4 photoelectrons/MeV into two APD's. There is an excess noise factor in APD's due to correlated gain in the device. This gives them effectively a factor of two fewer photons. Thus in CMS, photostatistics gives a contribution of $2.3\%/\sqrt{E}$. The term for lateral containment is based on 21.5 mm^2 crystals and a 5x5 clustering algorithm. They find a term $1.5\%/\sqrt{E}$. Adding these together in quadrature gives $2.7\%/\sqrt{E}$. CMS estimates a constant term of 0.55%. They also include extra noise due to leakage currents in the photodiodes, and the effect of summing over $\approx$25 interactions per crossing each with 7 times more energy than the Tevatron. We do not have these later effects at a significant level.

Additional guidance can be found by viewing the performance of the KTeV CsI calorime-

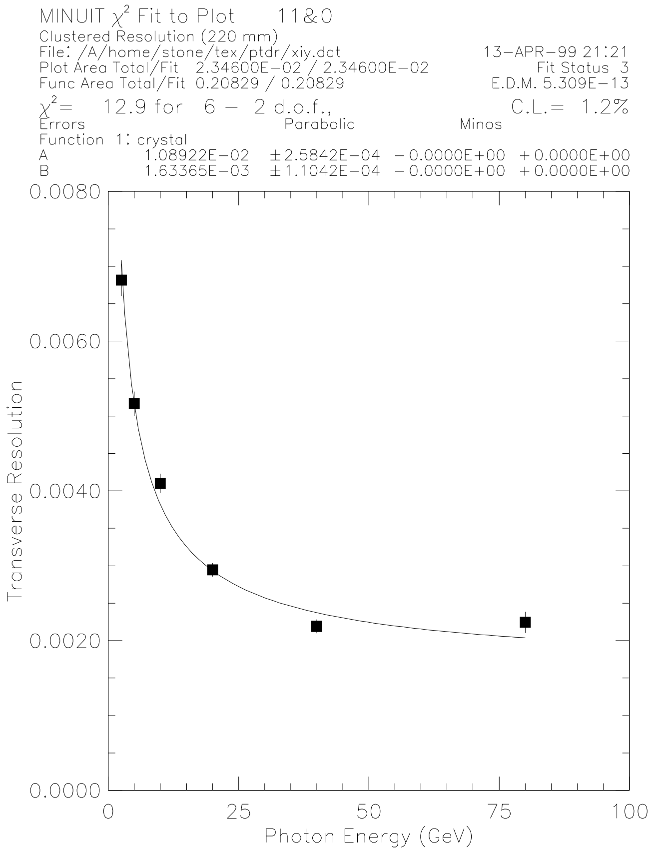

Figure 4.35: Energy resolutions as a function of incident photon energy for 220 mm long crystals using 5x5 clustering.

ter. They have achieved [3]

$$\sigma_E = \frac{2\%}{\sqrt{E}} \oplus 0.45\%. \tag{4.7}$$

The dominant cause of the constant term seems to be a differing crystal response depending on where on the face of the crystal the incident photon strikes. This effect was not observed in the CLEO CsI calorimeter [4].

The photon statistics term for BTeV, taking 7 photoelectrons/MeV is expected to be $1.2\%/\sqrt{E}$. We have already shown that the effect of transverse and longitudinal leakage in 220 mm long crystals is $1.1\%/\sqrt{E}$. Adding these two non-correlated components in quadrature gives $1.6\%/\sqrt{E}$. We have less knowledge of the constant term so we take the CMS estimated value of 0.55%. The expected energy resolution in BTeV then is

$$\sigma_E = \frac{1.6\%}{\sqrt{E}} \oplus 0.55\%. \tag{4.8}$$

To be conservative the physics simulations have been done using 2.5% rather than 1.6%.

iii. $\gamma - \pi^o$ Overlap

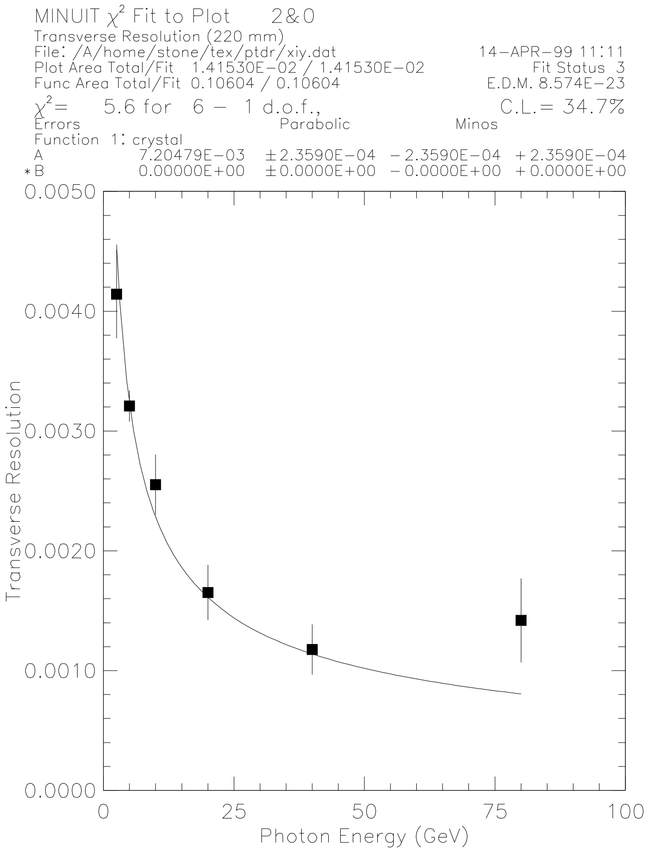

Figure 4.36: The contribution to the energy resolution from transverse leakage using a 5x5 array of crystals of 220 mm length and 24.7 mm^2 in cross-section.

It is clearly quite important for BTeV to be able to distinguish photons from π^o's. Many of the π^o's will be fast and could in principle appear as single photons. To study how well we could separate these two components with the proposed transverse segmentation, we generated both of them at fixed energies letting the $\pi^o \rightarrow \gamma\gamma$. We assumed only 4 photoelectrons/MeV, and a constant term of 0.55% thereby forcing a poorer energy resolution than we may achieve.

To study the probability of overlaps quantitatively, we calculate the second-moment of the energy distribution, S_2, defined as

$$S_2 = \frac{\sum_i \left(\overrightarrow{R}_i - \overrightarrow{R}_0\right)^2 \cdot E_i}{\sum_i E_i}, \tag{4.9}$$

where $\overrightarrow{R}_i$ is the position vector to the center of each individual crystal in the cluster, $\overrightarrow{R}_0$ is the energy weighted position vector of the entire cluster, and E_i is the energy deposited in each crystal. The S_2 distribution for both photons and π^o's of fixed energies is compared in Fig. 4.37.

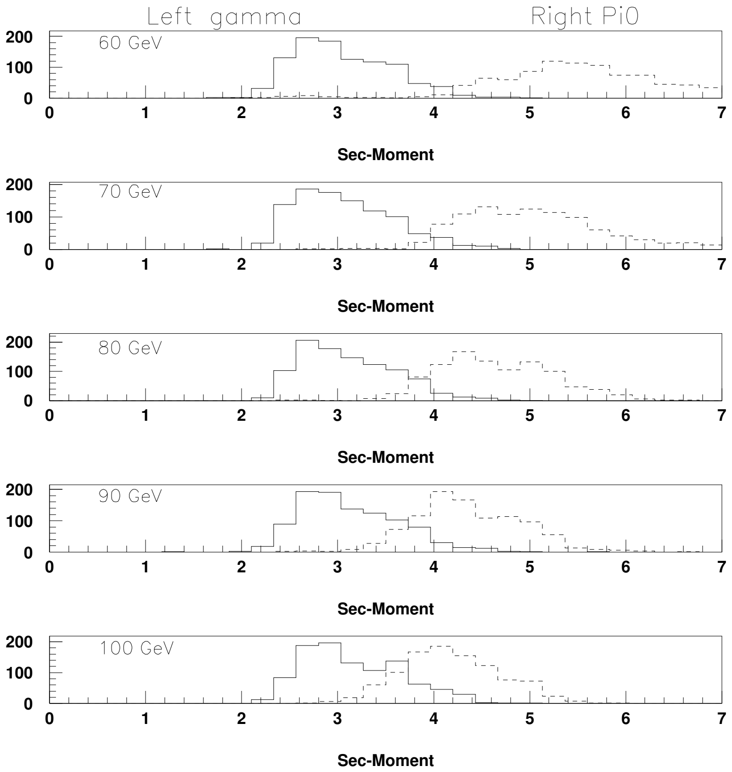

Figure 4.37: Second-moment energy distribution, S_2, for γ's and π^o's, as derived using GEANT and 4 photoelectrons/MeV.

In Table 4.12 we show the mis-identification rates for $\pi^o \rightarrow \gamma$ and $\gamma \rightarrow \pi^o$, both for 90% efficiency.

As most of the photons and neutral pions of interest in BTeV are below 60 GeV, the performance of the calorimeter in separating them is excellent.

iv. Position Resolution

The electromagnetic calorimeter is 7 meters from the center of the magnet. The resolution on projected angle is given in first order by the error in transverse position divided by 7 meters. The angular resolution enters directly in the mass resolution of fully reconstructed b and charm final states.

We again used GEANT to simulate the energy deposit in 220 mm long crystals taking 7 photoelectrons/MeV. Positions were then determined in both directions transverse to the crystal axes. As we have not seen any difference in the two directions, an advantage of square cross-section crystals, we show results only for one direction, called x. The position of the

Table 4.12: Neutral Particle Fake Rates for 90% Efficiency

Energy (GeV)	π^o to γ fake rate (%)	γ to π^o fake rate (%)
60	2.9	0.8
70	1.3	2.9
80	4.2	5.9
90	13.9	16.0
100	38.5	30.7

reconstructed photon is determined from the energy deposit by using

$$Xcl = \frac{\sum_{i=1}^{5} x_i \cdot E_i}{\sum_{i=1}^{5} E_i}, \tag{4.10}$$

where E_i is the energy reconstructed in each crystal, x_i is the center of each crystal and the sum extends two crystals in the direction of $-x$ from the highest energy crystal to two crystals in the $+x$ direction.

In Fig. 4.38 Xcl is shown versus the known position of the photon, $X0$ for 30 GeV incident photons. The characteristic "S-curve" shape is apparent. To evaluate the position resolution, the overall shape is removed by a fit and the remaining width of the curve gives the position uncertainty. In Fig. 4.39 the central value of the S-curve has been removed and the distribution in $dx = Xcl - X0$ fit with a Gaussian. The width of the distribution then is the r.m.s. position resolution.

The results of performing this study over a range of energies is shown in Fig. 4.40, where we show the r.m.s. position resoluton as a function of energy. The fit gives

$$\sigma_x = 3526\mu\text{m}/\sqrt{E} \oplus 217\mu\text{m}. \tag{4.11}$$

The projected position resolution then is much better than that assumed in the simulations, $\sigma_x = 247$ mm$/\sqrt{12} = 7100$ μm. These position resolutions give excellent angular resolution. At 6 GeV, the projected r.m.s. angular resolution is 0.2 mr.

4.2.6.9 Baseline Design

The baseline BTeV electromagnetic calorimeter consists of two wheels of 2.47 cm X 2.47 cm blocks of $PbWO_4$ crystals – one in each arm of the spectrometer. Each wheel is split down the middle to accommodate the beam pipe and to allow it to be moved away from the IR for servicing if necessary. The block length is chosen to be 25 radiation lengths (22 cm). We consider two options. They differ only in outer radius. The inner radius for both options is currently chosen to be 7 cm, which corresponds to ±10 mr. For the first option the outer radius is chosen to be 140 cm, which corresponds to 200 mr. The radius is less than we would like, but costs less. The total number of blocks is 10,000 per arm or 20,000 total. In size and

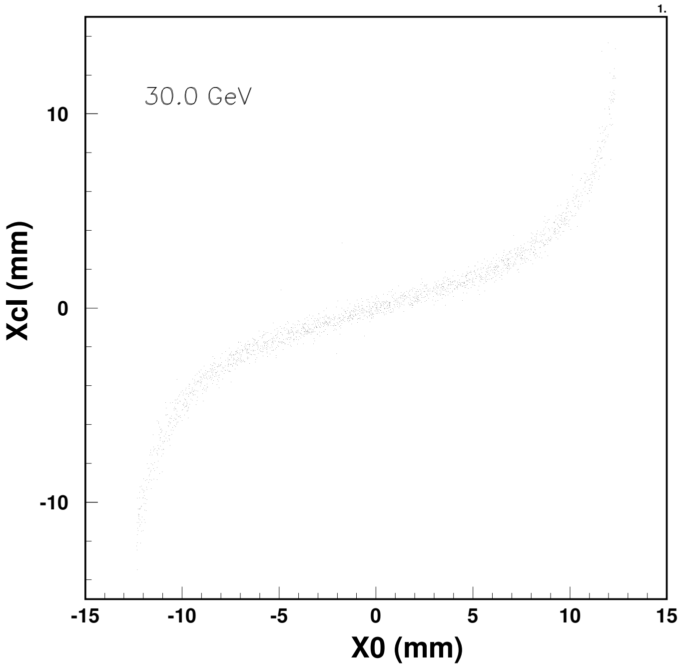

Figure 4.38: Measured photon position Xcl versus known photon position $X0$ for 30 GeV photons.

number of blocks, the system is only a little smaller than the CMS endcap calorimeter. It is this option that we call the baseline and have used in the simulations. The second option extends the calorimeter out to 300 mr. This is not only useful in getting more photon rate, but also extends the electron coverage. It does double the number of blocks, however, to 20,000 per arm.

At present, our blocks are rectangular solids. CMS has tapered its blocks so that the crystals almost point to the interaction point. We may consider doing this if further study shows it to be advantageous. The cross-section is chosen to be the same as the maximum size of the CMS end-cap blocks and the length is the same as the CMS endcap crystals.

There are detectors in each arm of the spectrometer. Each detector is housed in a temperature and humidity controlled hut. Temperature stabilization or some kind of correction is necessary because of the thermal coefficient of the $PbWO_4$. CMS plans to control the temperature to 0.1^oC. We will also employ temperature stabilization but have not yet designed the system. In addition to temperature stabilization, the gains are monitored with a laser pulsing system.

Detectors are read out with PMTs. The light emitted by the crystal peaks at 440 nm. The output of the PMT will go to a modified QIE chip located in or near the photomultiplier base. This chip provides a pulse height for each beam crossing. The expected light output is

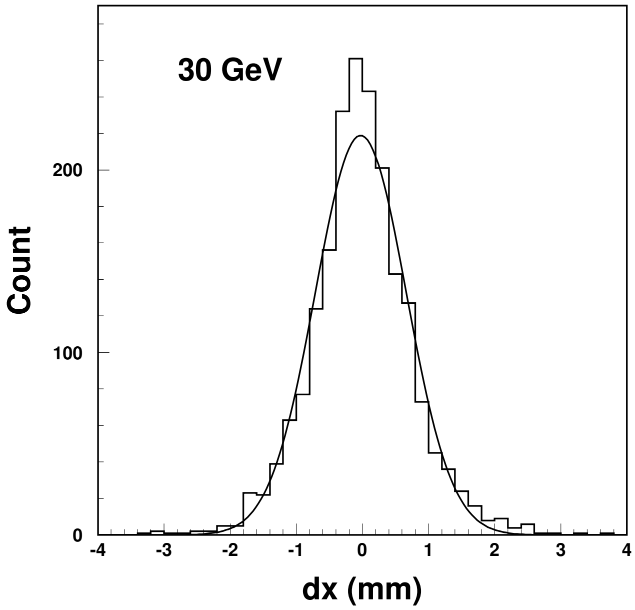

Figure 4.39: Distribution of $dx = Xcl - X0$ for 30 GeV photons. The fit is a Gaussian with mean consistent with zero and $\sigma = 0.7$ mm.

7000 photoelectrons at 1 GeV. The minimum sensitivity of the system is set so that a muon transversing the system, which corresponds to an energy deposition of 300 MeV, will have peak 50 counts above pedestal.

The detector is far enough away from the BTeV dipole so that there should be no need for special magnetic shielding. It is possible that we will magnetize the iron of the muon filter just downstream of the detector. In that case, we will put an iron shield plate between the calorimeter's PMTs and the muon filter.

Based on our extrapolation of information from CMS on the energy resolution, and our own GEANT studies, we expect a stochastic term of about 1.6%. The constant term is expected to be about 0.55%. The spatial resolution in both directions transverse to the Tevatron is expected to be about 3500 $\mu m/\sqrt{E} + 200$ μm, E in units of GeV.

Tests by CMS have indicated that these blocks can sustain integrated doses of 200,000 Grays. The only blocks that receive doses close to this number are the blocks right near the beam.

We have not yet started engineering on the support, but our detector is similar in size and shape to the CMS endcap electromagnetic calorimeter. A solution similar to theirs should work for BTeV. Because our detector is not embedded in a large device, and because at least at present we do not plan to use tapered blocks, our supports will be simpler and less expensive than those for CMS.

The properties of the baseline detector are summarized in Table 4.13. The GEANT studies described above demonstrate that the proposed device will satisfy the requirements of Table 4.9.

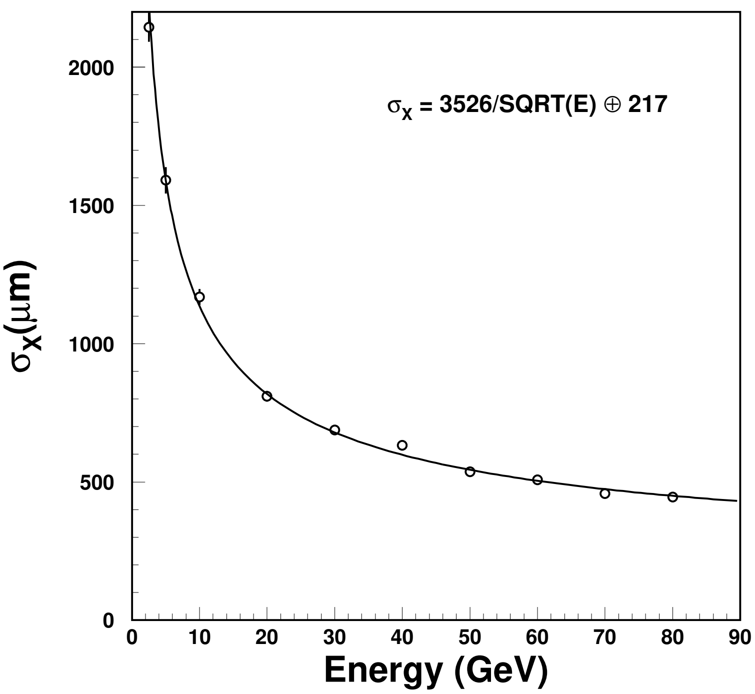

Figure 4.40: The expected r.m.s. position resolution for photons as a function of energy.

4.2.6.10 BTeV Electromagnetic Calorimeter R&D Program

At the time of our original R&D proposal, we did not have a plan for the Electromagnetic Calorimeter. We just listed several options, each of which had problems. Many of the problems we were worried about have been resolved by the development by CMS of $PbWO_4$ crystals as a viable calorimeter technology. We are taking full advantage of the work that CMS has done. We do have to carry out some R&D because we want to use photomultipliers rather than avalanche photodiodes. We will also be using a modified version of the QIE chip to read the data out. We want to obtain a few crystals and to try them with different types of PMTs and with QIE readout. We will have to explore cost issues with phototube manufacturers. Eventually we will want to expose a 5X5 (or better 7X7) stack of crystals to a low energy electron beam to study the resolution, leakage, temperature sensitivity, etc.

It is also critical that we begin to understand the issues related to producing crystals for BTeV. We will need to visit the existing production sites as well as to explore the possiblity of producing crystals with other manufacturers.

Table 4.13: Properties of the BTeV electromagnetic Calorimeter

Property	Value
transverse block size	2.47 cm X 2.47 cm
Block length	22 cm
Radiation Length (cm)	25
Front end electronics	PMT
Digitization/readout	QIE (FNAL)
Inner Dimension	$\pm$ 9.88 cm $\times$ $\pm$ 9.88 cm
Outer Radius (baseline)	140.0 cm
Total blocks per arm (baseline)	10000
Total blocks per arm (option)	20000
Outer Radius (option)	215.0 cm

Bibliography

[1] CMS, "The Electromagnetic Calorimeter Project Technical Design Report," CERN/LHCC 97-33, CMS TDR 4 (1997).

[2] T. Skwarnicki, "A Study of the Radiative Cascade Transitions Between the Upsilon-Prime and Upsilon Resonances," DESY F31-86-02 (thesis, unpublished) (1986).

[3] Private communication from Ed Blucher.

[4] E. Blucher, B. Gittelman, B. K. Heltsley, J. Kandaswamy, R. Kowalewski, Y. Kubota, N. Mistry, A. Bean, and S. Stone, "Tests of Cesium Iodide Crystals for an Electromagnetic Calorimeter," Nuclear Instruments & Methods **A249**, 201 (1986).

4.2.7 Muon Detection

The BTeV muon system has two primary functions:

- J/ψ and Prompt Muon Trigger: Besides providing interesting physics, this trigger performs an important service role by selecting (bottom) events on which the more aggressive and technically challenging triggers (such as the vertex trigger) can be debugged and evaluated.
- Muon Identification: Many of the experiment's physics goals (rare decay searches, CP violation studies which require tagging, studies of beauty mixing, searches for charm mixing, etc.) rely on efficient muon identification with excellent background rejection.

We have selected a magnetic (toroidal) design combined with fine-grained tracking elements (described in detail in a subsequent chapter). This design permits "stand-alone" momentum/mass triggering: *i.e.* a muon trigger based solely on information from the muon detector. In addition, improved background rejection is possible via comparisons of this stand-alone measurement with momentum and tracking information from the rest of the spectrometer. The design of the system, including the fine-grained detector segmentation, has been chosen to reduce and uniformly distribute occupancies and to minimize confusion in pattern recognition (both at the trigger level and in offline reconstruction).

In order to provide a viable trigger, the system must get a rejection at Level 1 of a few 10^{-2}. The goal for muon misidentification is 10^{-3}.

Given the objective of a "stand-alone" trigger and the size limitations set by the experimental hall, one can make fairly general calculations that place specific (and restrictive) constraints on the design of the system. We will first describe these general calculations and use them to motivate the overall design of the muon system. We will then describe trigger efficiency and rejection studies we have performed for $B^0 \to J/\psi K_s^0$, which illustrate the performance of the design for a specific (and important) physics mode.

4.2.7.1 General Design Considerations

In the absence of any special momentum dependent coordinate weighting designed to reduce the effects of multiple Coulomb scattering, the fractional momentum resolution in a magnetic spectrometer can be parameterized by the expression:

$$\frac{\sigma_p}{p} = \sqrt{a^2 + (b\ p)^2} \tag{4.12}$$

In Equation 4.12, the a term depends on the bending power and multiple scattering environment of the detectors, while the b term depends on the bending power and and the detector layout and spatial resolution. Fig.4.41 shows that the potential rejection provided by a trigger for low momentum muons significantly degrades once the low momentum fractional resolution exceeds 25%. An $a = 25\%$ value means that the trigger rejects very soft muons at roughly the 4σ level. At higher momentum, where multiple scattering is less important,

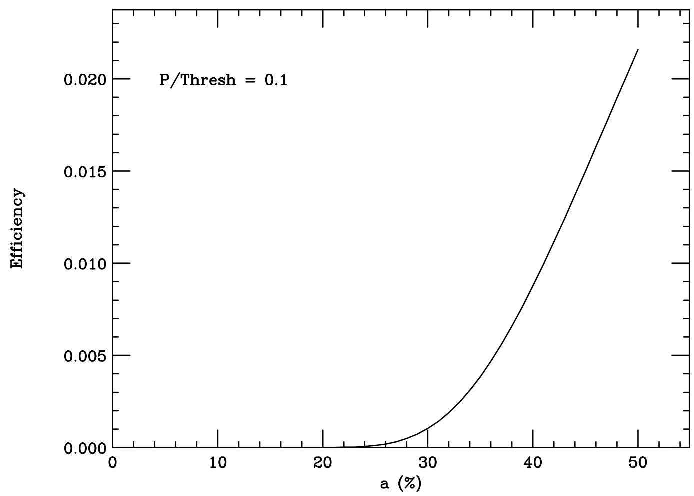

Figure 4.41: The efficiency, calculated in a simple Gaussian model, for a muon with 1/10 the threshold momentum to pass a momentum threshold as a function of a, the MCS term in the resolution formula. We say that a muon at the threshold momentum should fire the trigger 50% of the time. Note the dramatic rise in sensitivity above $a = 25\%$.

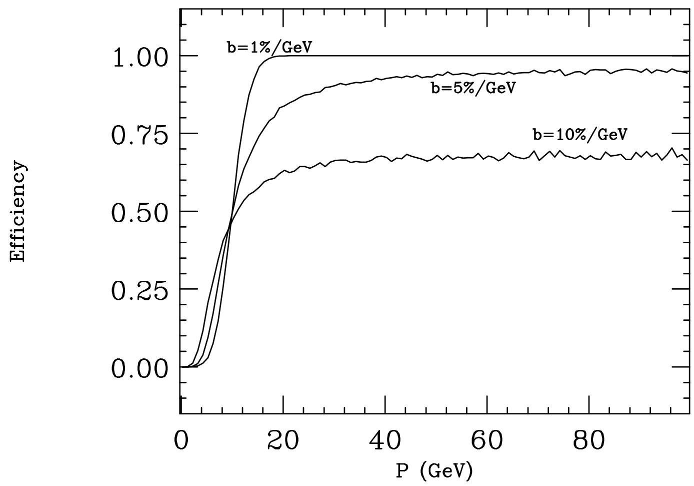

Figure 4.42: Simulated trigger efficiency as a function of muon momentum for a trigger designed to fire with a 50% efficiency at 10 GeV. The multiple scattering dominated term is set to $a = 25\%$ while the measurement dominated term varies from $1\%/GeV < b < 10\%/GeV$.

one becomes sensitive to the b term of Eq. 4.12. The high momentum resolution influences how sharp a momentum threshold one can make in a stand-alone muon trigger. Figure 4.42 illustrates this point by showing the trigger efficiency as a function of momentum for several b values.

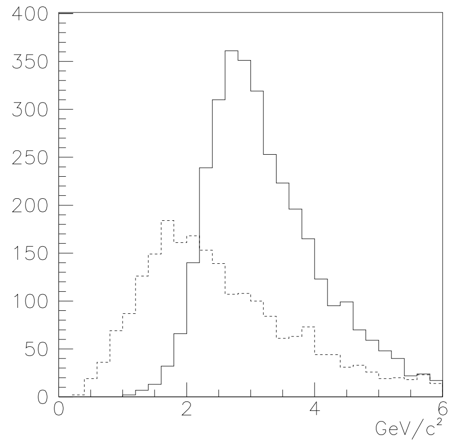

Figure 4.43: Reconstructed $J/\psi \rightarrow \mu^+\mu^-$ mass resolution for $b = 1\%/GeV$ (solid) and $b = 5\%/GeV$ (dashed), where b is defined in Eq. 4.12. Equal numbers of J/ψ candidates were generated for each case.

These considerations suggest minimum performance criteria of $a < 25\%$ and $b \leq 1\%/GeV$. As a further illustration, Fig. 4.43 shows the mass resolution obtainable at the trigger level for $J/\psi \rightarrow \mu^+\mu^-$ events for two values of b.

4.2.7.2 Possible Design Layouts

Several possible measurement and shielding layouts were studied before we reached the baseline design. In assessing possible layouts, we compute the momentum resolution using an error matrix which incorporates Gaussian models for both the detector resolution and multiple Coulomb scattering. The beam is modeled as a Gaussian beam spot with $\sigma_x = \sigma_y = 1$ mm and $\sigma_z = 30$ cm. In cases where there is redundant coordinate information, the error matrix assumes that the fit weighted the space points according to momentum in order to get the best possible momentum measurement.

Our early calculations showed that it is not possible to get a good momentum measurement using just the dispersion provided by the central dipole (and a constraint that muon system tracks point back to the interaction point). The extrapolation distance is too large given the level of multiple scattering up to the muon planes, making it infeasible to point the muon track segment back to the interaction region. A magnetic toroid with magnetic fields circulating in the $\hat{\phi}$ direction is the only (simple) option which allows us to trigger effectively using tracking information from only the muon system.

The first arrangement we considered is illustrated in Figure 4.44. In this design, one determines the momentum of a muon by measuring its slope in $\hat{\theta}$ before and after a toroid. The entering and exiting slopes of the muon are measured using two pairs of measuring stations (μ_1–μ_4) separated by one meter lever arms. At low momentum, where the multiple scattering dominates resolution, a single 1.5 Tesla, 1 meter thick toroid achieves the required

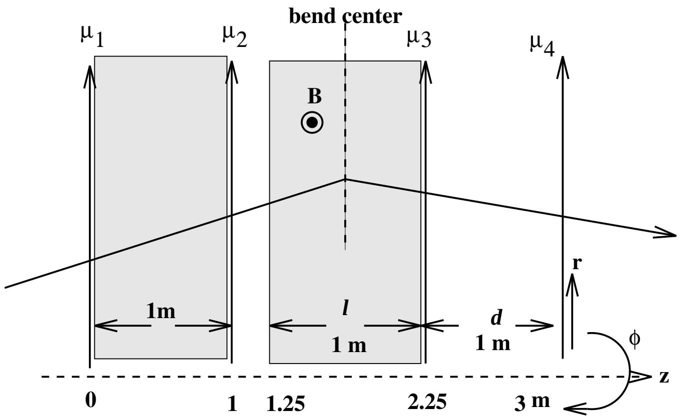

Figure 4.44: Layout of one arm of the muon detector in $2 \oplus 2$ geometry.

fractional momentum resolution of $a = 25\%$. In this arrangement the steel between the measurement stations of the upstream doublet (μ_1–μ_2) primarily serves to shield the muon system from hadrons and need not be magnetized. The requirement of good momentum resolution ($b \approx 1\%/GeV$) dictates a spatial resolution of $\sigma = 2.5$ mm. We will call this the "$2 \oplus 2$" geometry.

Note that the intrinsic rms spatial resolution ($\sigma = 2.5$ mm) required by this (and subsequent) geometries is consistent with what we require from timing considerations alone. Timing information is useful for rejecting background hits such as those associated with accelerator backgrounds (these hits come 60–70 ns before tracks from the interaction point). Assuming a fast gas drift velocity of roughly 9 cm/μs, a drift tube system with a maximum drift time of 30 ns has a maximum drift length of 2.5 mm (leaving 30 ns for charge integration). For a double layer of 1 cm diameter round proportional tubes, offset by half a tube in a "picket fence" design (to avoid dead regions between the tubes), the maximum drift time for the first signal from a track is 30 ns. This arrangement yields an rms resolution of $\sigma = 1.44$ mm.

The major problem with the $2 \oplus 2$ design is that the most upstream of the four detector stations is unshielded against hadronic showers originating in the electromagnetic calorimeter and is thus likely to be too confused for use in a first level trigger. One could, in principle, measure momentum using the downstream doublet μ_3 and μ_4 and a single upstream point μ_2. This geometry gives essentially the same a parameter, but for the same spatial resolution the b parameter is degraded by a factor of 2.8 because the effective upstream lever arm has been reduced to just the distance between the bend center and μ_2.

This led us to the revised design, our "baseline" geometry, illustrated in Fig. 4.45 where the upstream muon trajectory is measured using information from the nominal beam constraint. The effectiveness of this approach is illustrated in Fig. 4.46. The upper black curves give the fractional momentum resolution as a function of muon momentum for the case where only the downstream steel is magnetized and only information from μ_3, μ_4 and the nominal beam center is used. The three curves are for muons emerging at three different azimuthal

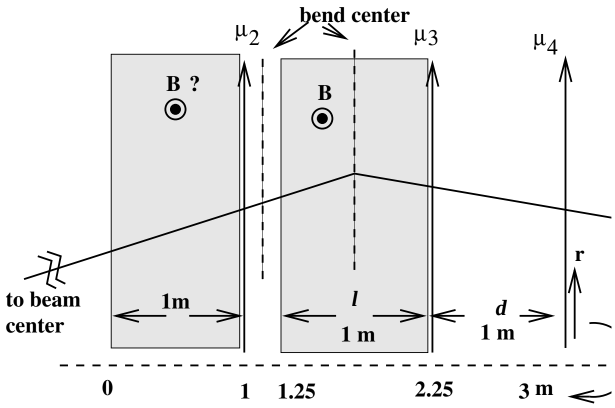

Figure 4.45: Layout showing the baseline geometry. The downstream trajectory is measured by μ_3 and μ_4. The upstream trajectory is measured using the nominal beam center with possible help from μ_2. In order to get sufficient bending power, both steel sections will need to be magnetized.

(ϕ) angles. The pronounced azimuthal variation in fractional momentum resolution arises because of constructive and destructive interference between the dipole and toroid fields. Figure 4.46 shows that at destructive ϕ angles, the a term exceeds our criteria of $a < 25\%$.

The incorporation of information from μ_2 significantly helps the fractional momentum resolution for the case of a single toroid at low momenta as shown in the three blue curves of Fig. 4.46. Essentially the fit used to obtain the "blue" resolution curves ignores the beam constraint at low momentum while exploiting it at high momentum through momentum varying weights. Such a resolution is obtainable off-line, but would be difficult to achieve in a first level trigger.

If one instead magnetizes both the upstream and downstream steel, the bending power of the toroid overwhelms the power of the dipole and a much simpler triggering scenario emerges which is illustrated by the lower seven curves of Fig. 4.46. The case where only a beam constraint and μ_3–μ_4 are used in the trigger is illustrated by the dashed red curves. The green curve shows the resolution one would obtain using a beam constraint and the downstream μ_3-μ_4 doublet if the central dipole were turned off. The green curve shows that the dipole provides very little additional bending power in the ultimate system. When information from μ_2 is included one gets the solid magenta curves. Again, curves are shown for three different azimuths. Each of these curves exhibit good performance relative to our criteria on a and b (over the complete azimuth).

Interestingly enough, Fig. 4.46 tells us that in a two magnet, toroid geometry, μ_2 contributes very little to the momentum resolution. In the absence of noise or confusion, one can design a very simple but effective trigger by correlating information from just the two $\hat{\theta}$ views of the downstream doublet consisting of μ_3 and μ_4 and the nominal beam center. Since this is the minimal amount of information required to obtain a momentum estimate, no momentum dependent weighting of detector information is used. We also have the benefit of deriving this trigger from the most shielded chambers of the muon system, minimizing

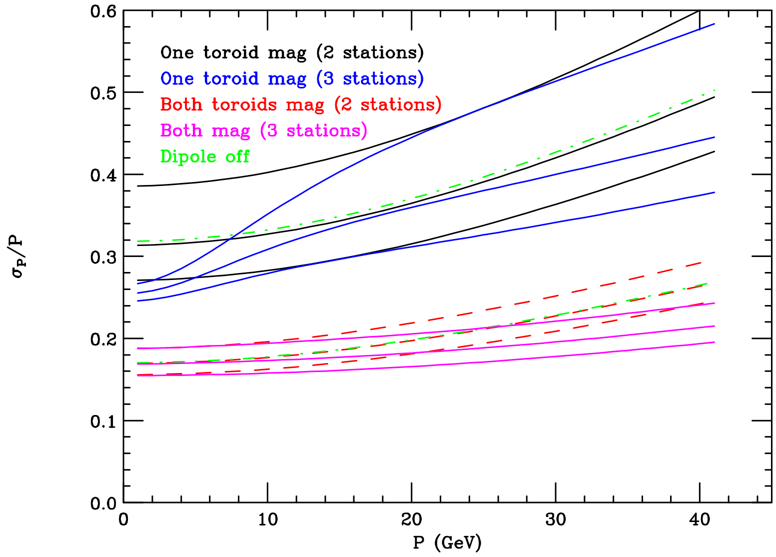

Figure 4.46: Plots of the fractional momentum resolution as a function of momentum for various readout scenario's of the BTeV muon system. All plots assume chambers with 2.5 mm rms spatial resolution. The plots appear in groups of 3 corresponding to $\phi = 270^o$ (best) 0^o and 90^o (worst). The ϕ dependence of the resolution illustrates interference between the central dipole and muon toroid(s). The black and red families of curves illustrate the case where only the two stations after the second toroid are used in the trigger. In this case the trajectory upstream of the toroid comes entirely from the beam constraint. The blue and magenta curves illustrate the case where the station between the two toroids is used to help determine the trajectory prior to the toroids. The green curves assume only the final two stations are used, and that the dipole is turned off .

hadronic punch-through effects.

Although μ_2 is not required to measure muon information in our two toroid scenario, it is likely to be of substantial use in eliminating false triggers due to noise and confusion. Figure 4.47 illustrates just one example by showing how μ_2 can be used at the trigger level to eliminate false triggers from soft muons with an accompanying δ-ray.

4.2.7.3 Baseline Design

Based on the above, our baseline muon system consists of two 1 m thick iron toroids and three measurement stations with spatial resolutions of $\sigma = 1.5$ mm. Each of the measurement stations is separated by approximately 1 meter. The spatial resolution is set by both timing considerations and momentum resolution requirements.

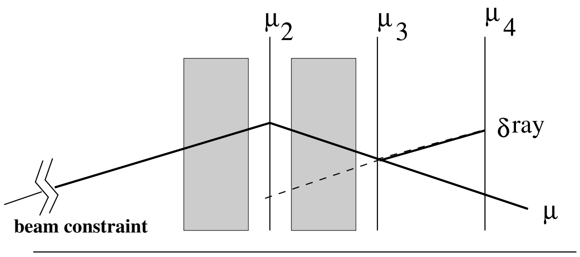

Figure 4.47: This figure illustrates the usefulness of μ_2 in reducing false triggers due to confusion from δ-rays. We illustrate a trajectory for a low momentum μ which is severely bent by the two toroids and therefore extrapolates far from the nominal beam center. As this muon emerges from μ_3 it emits a wide angle δ-ray which leaves an additional hit in μ_4. In the case illustrated, the two hits in stations μ_3 and μ_4 from the δ-ray point back to the nominal beam center and mimic a high momentum muon. However, the δ-ray trajectory extrapolates very far from the muons hit in μ_2 and thus fails to satisfy a trigger which requires a confirming hit in μ_2.

4.2.7.4 Trigger Studies for $B^0 \to J/\psi K_s^0$

We have studied the triggering performance of our baseline muon system using MCFAST. We used minimum bias events to study rejection ratios and $B^0 \to J/\psi\, K_s^0$, where $J/\psi \to \mu\mu$, to investigate trigger efficiency. The minimum bias events were generated with Pythia and include elastic scattering, single and double diffractive, low p_T scattering and semi-hard QCD $2 \to 2$ processes. Events are overlapped to simulate multiple events per crossing. The number of events per crossing is generated from a Poisson distribution with average two. In generating the $B^0 \to J/\psi\, K_s^0$ events, minimum bias events are also added so that the total number of interactions per crossing is also Poisson with an average of two. For the studies presented below, we only consider "real" muons, which can be prompt or can come from decays in flight. In minimum bias events, the muons come almost entirely from pion (70%) and kaon (30%) decays. "Fake" muons from punch through, delta rays, and noise hits in the chamber are not yet simulated.

In the calculations below, efficiency is the ratio of accepted events to generated events. This includes geometrical acceptance and the selection cuts. For our purposes, a signal ($B^0 \to J/\psi\, K_s^0$) event is considered to be in the geometrical acceptance if both tracks from the J/ψ muons are tracked by the silicon and make it through all stations of the muon system. The muon system is assumed to have an outer radius of 2.4 m and the inner radius is varied between 10 cm and 20 cm (10 cm is the smallest possible inner radius given the inner radius of the toroids, while 15–20 cm is the smallest inner radius that can probably be achieved with the baseline design). At that point, both minimum bias and signal events are treated identically. They are accepted if muon(s) in the event pass cuts on momentum, transverse momentum, and/or a minimum invariant mass cut on muon pairs. In all cases where two muons are required, they must have opposite sign and be in different octants in ϕ (each detector plane in the baseline muon system is divided into eight pie shaped octants).

The pair of muons must also be in the same arm of the detector.

The momentum and transverse momentum of each muon in the event is obtained by smearing its generated momentum using the appropriate resolution (see Fig. 4.46) and smearing function. We then vary the cuts on momentum, transverse momentum, and invariant mass of pairs of muons and make two dimensional plots showing rejection of minimum bias events on one axis and J/ψ efficiency on the other. An example plot is shown in Fig. 4.48. We have made similar plots for differing inner radii, one versus two toroids, and so on. Based

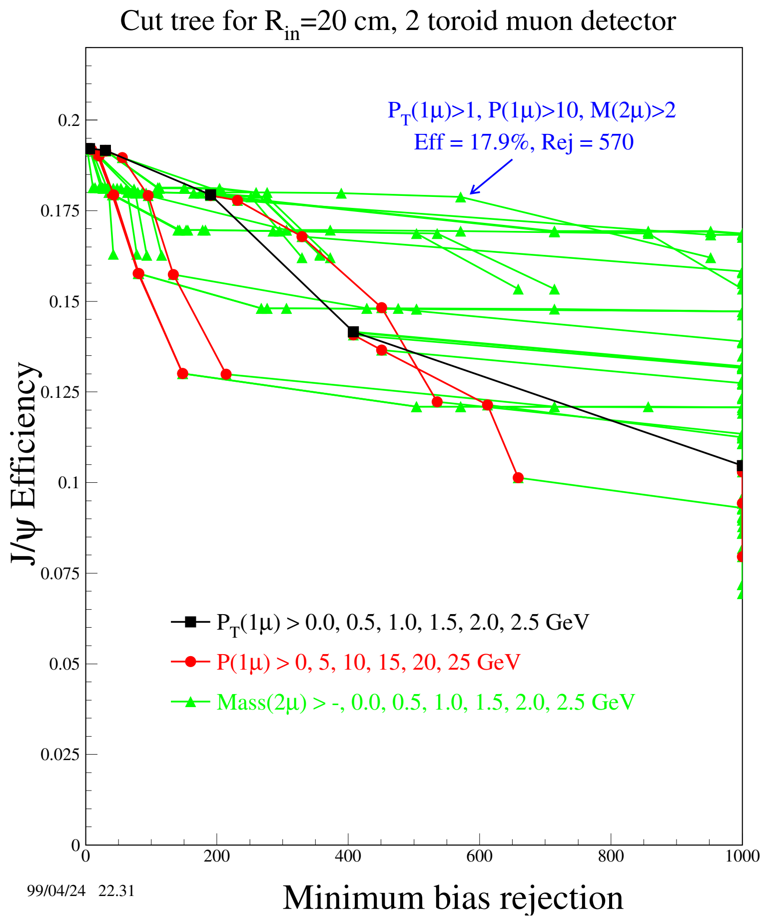

Figure 4.48: Absolute J/ψ efficiency versus minimum bias rejection for cuts on the minimum muon p_T, the minimum muon momentum and the minimum invariant mass. Black lines connect the squares which show the variation as the minimum muon p_T is increased. From each black square a red line connecting the circles shows the change as the minimum muon momentum is increased. From each red circle a green line connecting the triangles shows the variation as the minimum invariant mass requirement is increased. A cut of "-" indicates no cut. Results are for a two-toroid muon detector with inner radius of 20 cm.

on these studies, we find typical rejection ratios of 500-600 with efficiencies of roughly 18%. Note that the geometric acceptance (no momentum or mass cuts) of a 10 cm inner radius system is 22%. Based on these studies, we have found:

1. Most of the rejection power comes from requiring minimum p and p_T for two muons in the event. An invariant mass cut is beneficial, but is not required to obtain large rejections with good efficiency. If it turns out that an invariant mass cut is difficult to implement in the first level trigger, we will not be at a severe disadvantage.

2. An inner radius of 15–20 cm is acceptable. If we insist on a rejection ratio of 500 or more, the efficiency for signal events is 18.8% for an inner radius of 10 cm and 17.9% for an inner radius of 20 cm (20 cm is worst case).

3. Two toroids are needed. If we require a rejection ratio of 500–600, the efficiency for signal events drops significantly (from $\sim$18% to $\sim$14%) in going from two toroids to one. In fact, it appears that the only hope for a single muon trigger is the two toroid case: acceptable rejections are not possible with only one toroid.

4.2.7.5 Summary of Detector Requirements

To summarize, the BTeV muon system should have the following attributes:

1. Robust: It will be very difficult to access the detectors once they are installed.

2. High Rate Capability: Rates of a few kHz/cm^2 are possible in parts of the system (based on calculations of accelerator backgrounds).

3. Good Time Resolution: Timing information on hits with a resolution of 50–60 ns will allow rejection of hits due to accelerator backgrounds.

4. Magnetic: Two toroids of 1.5 Tesla field and roughly 1 m thickness (in each arm).

5. Fine-Grained Spatial Resolution: Tracking resolutions of 2–3 mm are required.

6. Longitudinal Compactness: Given the size constraints, the detectors should be of minimal thickness.

7. Minimal Neutron Susceptibility: We will avoid the use of hydrogenic detector elements.

8. Uniform Occupancy: A geometry designed to minimize pattern recognition confusion and minimize occupancy at smaller radii.

The details of the baseline muon system design are discussed in a subsequent chapter.

4.3 Evolution of the C0 Program

We want to congratulate Fermilab on the completion of a new experimental area at C0 which is capable of supporting a state of the art bottom and charm decay experiment. We have carefully designed BTeV to be a good match to this new enclosure. We propose to develop the experiment in stages. Some of these stages involve R&D into key technologies required for the experiment. Others involve a program of physics and background measurements. Only by doing tests under actual running conditions does one truly confront all the problems of efficiency, backgrounds, and systematic errors in the design.

The rate at which the full experiment can be mounted depends on many things. One is when the lowβ quadrupoles will be available, since this determines the earliest time when we can have collisions at high luminosity. Another is when the R&D for each component is completed. A third is, of course, when manpower for design work and money to build detectors and buy the electronics and computing become available. Finally, all the equipment must be installed, integrated, and made to work.

We assume that the running schedule around which we plan our activities is: each year there will be about 9 months of collider running; that there will be a three month shutdown for maintenance during which installation can take place; and that at some point after a few years of running, the 3 month shutdowns will be arranged back-to-back so that there can be a reasonable period for envisioned upgrades.

Our first goal is to get the 'large components' installed in C0 during the shutdown for Run II installation. At the minimum, this means the SM3 analysis magnet. If we can locate the steel for one or both of the muon detectors, we would like to get that installed too. Once these components are in, all other installation activities are similar to installing components in a fixed target experiment. Individual modules of the detector can be moved into the enclosure and installed in short shutdowns of a few days.

BTeV R&D is proceeding well. Pixel R&D is well along and we would like to complete it in 2002. Two different readout chips, bump-bonded to detectors will be tested in the 1999 fixed target run. Trigger R&D is also proceeding well and will be completed in 2001. The design of the forward tracking system, muon chambers, particle identification system, and electromagnetic calorimetry can be completed in 2001. Prototype modules of the forward tracker and the muon chambers will be tested in the 1999 fixed target run.

Starting at the beginning of Run II we will put counters into C0 to measure backgrounds near the IR and in the region of the muon detector and RICH; to set up the prototype modules of the muon detector and the forward tracker and operate them in the C0 enclosure; to install a wire target and study the interaction rate and backgrounds, and establish the effect on the other collision regions.

In 2000, we also plan to install three pixel planes inside the SM3 magnet and several forward tracking planes, along with trigger scintillators. We will use this arrangement to study the initial full size pixel detector chips in a prototype housing inside the beam pipe. Interactions on a wire target will be used. We are also proposing to establish the ability to test electronics near the beam by placing them in existing Roman Pots.

We plan to have our first $p\bar{p}$ collisions in 2002 using an intermediate $\beta*$ IR constructed from existing quadrupole magnets. This arrangement will not permit us to run simultaneously with both CDF and D0 since separators will need to be turned off to bring the beams into collision at C0. We envisage intermittent running perhaps using the ends of stores. We will install 10% of the final pixel system, a serious full scale system test of both the pixels and the trigger. We will also measure the backgrounds in the collider mode. We will interleave wire mode and collider running and test as much of the vertex tracker and vertex trigger as possible.

In 2003 we plan to start installing the rest of the BTeV spectrometers, and have some collider running after each installation period.

We look forward to full runs in collider mode building up to full luminosity in 2004 and 2005.

With this plan, we can steadily build our understanding of the detector over a period of a few years and can be ready to do physics with a tested analysis program in place when the full detector is complete. It also allows the lab to spread its resources, people and money, over several years. Following this plan, Fermilab will have a serious forward collider B experiment well in progress before the LHC turns on.

4.4 Completing the Simulation of the Baseline Detector

The simulation work on all-charged states is quite far along and has dominated the requirements for the baseline detector. The study of states with photons and π^o's has just begun. More physics channels will be investigated and background calculations for states with photons will be pursued aggressively even though they require us to run a very large number of events. The current baseline detector has been modeled and extensively studied and we are now confronting very detailed problems which involve more global optimizations – those requiring an understanding of the impact of various choices on the whole ensemble of physics topics. For example, the thickness of the pixel detector is a problem not so much for its effect on charged particle tracking but for its impact on photon reconstruction because so many photons undergo conversion to e^+e^- pairs.

We have also made much progress in improving the detail of the simulation and bringing it closer to reality. Significant design work is occuring on nearly all the detectors. As the design of the detectors begins to firm up, we are feeding information into the simulations to make them more realisitic with respect to cell sizes, resolutions, and material budget. Much of the work in the next year will be in modeling the details of the detector elements and understanding more complex issues and detector dependent issues such as pattern recognition and trigger rates to make sure that the proposed design can actually do the measurements we are interested in.

The trigger simulation includes pattern recognition in tracking the charged particles through the silicon detector. More detailed hit generation and digitization have been implemented so that we can more fully understand the efficiency and rejection of the trigger. We have begun to investigate other trigger algorithms as part of the trigger R&D effort. We are pursuing schemes with fewer planes to reduce the amount of material in the vertex detector and to reduce its complexity. Further simulations will be required to fully understand the effects of multiple interactions on the tracking and vertexing efficiencies although much work has already been done in this area. Serious work has been carried out on the Level 2 and Level 3 trigger algorithms and the overall trigger and data acquisition architecture.

Detailed simulations of the expected background rates in the C0 hall have not yet been performed. We will study backgrounds from all sources including those generated in the machine.

There are tools available to study the beam backgrounds [1]. Proton-antiproton collisions are typically simulated with DTUJET93. Beam halo interactions with scrapers and particle tracking through the Tevatron are modeled with STRUCT. Particle loss induced hadronic and electromagnetic showers, and secondary particle transport in accelerator and detector components, including shielding, are simulated using the MARS simulation package. We expect to carry out studies of the beam related backgrounds in cooperation with the Beams Division as the design of the detector and interaction region move ahead. We also are planning to undertake a series of measurements of the environment in the C0 Collision Hall as soon as collider operation resumes.

The simulation tools are now in place to study all the physics and detector issues that need to be addressed to make the final refinement of the BTeV detector. Over the next year, we expect to investigate a wide variety of physics topics and detector issues connected with bottom and charm physics and improve the background studies and to be in a position to make a final "global optimization" that will result in a final design that will give BTeV the greatest possible physics reach.

Bibliography

[1] From the C0 Workshop, Fermilab, Dec 4-6, 1996. See http://fnphyx-www.fnal.gov/conferences/czero/simulations_summary.html